Abstract

Title of Dissertation: ANALYSIS AND MITIGATION OF ELECTROMAGNETIC
NOISE IN RESONANT CAVITIES AND APERTURES

Lin Li, Doctor of Philosophy, 2004

Dissertation directed by: Associate Professor Omar Ramahi, Mechanical Engineering

The trend of low voltage in electronics circuits and boards makes them vulnerable to electromagnetic interference (EMI). Furthermore, higher speed (clock rate) leads to faster switching which increases the potential for higher radiation from circuits and boards. These inevitable trends collectively compromise the electromagnetic compatibility of electronic systems by increasing their electromagnetic susceptibility. In this work, radiation from enclosures and apertures is studies and characterized and radiation mitigation techniques are proposed.

High-speed circuit radiation within an enclosure leads to cavity resonance that can have critical impact on other electronic components housed within the same enclosure. The amplified electric field in the enclosure can couple to critical circuits leading to either hard or soft failures. One measure to gauge the resonance of an enclosure is through the determination of S-parameters between certain ports connected to the enclosure. In this work, different numerical methods for efficient prediction of S-parameters are proposed and evaluated for their effectiveness and accuracy. Once an

efficient procedure is established for calculating S-parameters, novel topological variations within the enclosure can be tested before manufacturing using accurate numerical prototyping. The proposed numerical S-parameters calculation algorithms are validated by comparison to laboratory measurements.

Radiation from resonant apertures present in the walls of enclosures represents a second major source for radiation. In this work, a novel analysis of aperture radiation is presented based on the interpretation of the aperture as a transmission line. Once the transmission line analogy is established, a novel aperture resonance mitigation technique is proposed based on the use of material coating that mimics the behavior of matching loads that typically terminate transmission lines. The technique consists of adding resistive sheets in selected places in, or around the aperture. The effectiveness of the proposed method is demonstrated by first using numerical simulation of an aperture present in an infinite perfectly conducting sheet, and then by designing an experiment where the novel technique proposed here is tested on resonant apertures present in a metallic box. Both radiation measurements in an anechoic chamber and S-parameters measurements were conducted to test the validity of the proposed mitigation techniques.

ANALYSIS AND MITIGATION OF ELECTROMAGNETIC NOISE IN RESONANT CAVITIES AND APERTURES

By

Lin Li

Dissertation submitted to the Department of Mechanical Engineering
University of Maryland, College Park in partial fulfillment of the requirements
for the degree of Doctor of Philosophy
2004

Advisory Committee:

Associate Professor Omar M. Ramahi, Chairman/Advisor
Professor Michael Pecht
Professor Victor Granatstein
Associate Professor Peter Sandborn
Associate Professor Patrick McCluskey

Acknowledgements

I owe my gratitude to all the people who have made this thesis possible and because of whom my graduate experience have been valuable to my future.

First and foremost I would like to thank my advisor, Professor Omar Ramahi for giving me an opportunity to work on challenging and extremely interesting projects over the past four years. He has always made himself available for help and advice. It has been a pleasure to work with and learn from such a knowledgeable and patient advisor.

My colleagues at the electromagnetic compatibility and propagation laboratory have enriched my graduate life in many ways. Mohammad Kermani helped me to do radiation test and material property test. Seokjin Kim provided help by setting up the vector network analyzer. Baharak Mohajeriravani worked with me to develop the post process for HFSS simulation.

I would also like to thank Dr. Bruce Archambeault for giving me the license of EZ-FDTD software. I should specially thank Professor Michael Pecht for leading me to the electromagnetic compatibility area.

I owe my deepest thanks to my family - my mother and father who have always encouraged me and relieved my pressure. My wife He Huang gave me all her best to support me to finish this work.

It is impossible to remember all, and I apologize to those I've inadvertently left out. Thank you all!

Table of Contents

List of Figures

Chapter 1 Introduction and Background

1.1   Cavity Resonance

Elementary microwave theory states the fact that any enclosure will resonate at certain frequencies. At resonant frequencies standing wave occurs when wave traveling back and forth such that they add constructively. For an electrically thin cavity, a standing wave inside the cavity will alter the wave impedances. If we assume metallic or conductive wall, the transverse electric field and hence the wave impedance will be zero while a quarter wavelength away the impedance becomes infinite provided there is no loss. The standing wave will affect the input or output impedances of the device drastically where the standing waves peaks and nulls occur. At these frequencies the resonance increases the likelihood that device will radiate extraneous energy especially at high frequencies.

The calculation of the resonant frequencies and field distribution of a rectangular cavity is fairly straightforward. However, a large cavity will have multiple resonance modes and frequencies. Knowledge of how the resonance is excited would be needed to fully determine the field distribution and this is often difficult if not impossible.

S-parameters can be used to quantify the resonance of a cavity. S-parameters can be measured experimentally by using a vector network analyzer. S-parameters can also be evaluated numerically, making it possible for complete numerical prototyping before actual construction of enclosures or cavities.

1.2   Aperture Radiation

Aperture geometry has long been studied in electromagnetics. Many efforts have been contributed to consider the electromagnetic waves propagation and penetration through apertures. The aperture and slot are structures commonly seen on varieties of electronic packaging especially on enclosure and chassis. The apertures of the chassis dominantly decide the system level shielding effectiveness. This work focuses on mitigating this radiation through apertures. The reduction of this unwanted noise would improve the electromagnetic compatibility (EMC) of enclosures.

The problem of radiation through apertures is one of the most classic in the physical sciences. In fact, the fascination with aperture radiation dates back to at least the European Renaissance [1]-[3]. Numerous papers have been published in the past fifty years that investigated the behavior of electromagnetic energy as it escapes through apertures. Some of these publications attempted to develop approximate analytical formulations, such as, for instance, the work of Bethe [3], Hill *et al.,* [4], and Ott [5], while other works were not constrained by the electrical size of the aperture and were primarily focused on developing analytical techniques that can be used for a class of aperture configurations [6]-[11], or efficient numerical techniques that can be used in general [12]-[18]. It is perhaps fair to state that most of the works that was published on the radiation of the aperture had to deal with either developing approximate formulae or numerical techniques to predict radiation through apertures.

The concern in this work is the energy going through aperture whether with cavity back or not, whereas the latter one has more practical implication. The chassis or enclosure of electronic devices has apertures for heat dissipation and input/out

interfaces. The integrity of shielding enclosures is compromised by aperture arrays for heat dissipation. The structure and techniques to reduce the radiation through aperture is a major interest for its importance to electromagnetic compatibility.

1.3 Absorbing Material

Applications for such materials include measures for reducing the radiated noise and improving the resistance of electronic devices (such as communication devices, office electronics, computers, home appliances, and devices mounted on automobiles), the attenuation of radio wave reflections, and facilities for evaluating EMI measures (such as anechoic chambers).

With the proliferation of telecommunications technology, the consequent push for electromagnetic compatibility and a general trend toward higher frequencies, electronics design is confronting unprecedented challenges. Material absorbers are now used in a variety of applications in the commercial marketplace. Absorbers are currently used for lowering the quality factor of cavities where microwave circuitry is operating, reducing the resonance in cavities. In this work, an effective technique is introduced to lower quality factor of cavity and radiation from resonant apertures.

Adding microwave absorbing material to a cavity has been a quick and inexpensive way to eliminate cavity resonances. From basic theory, the insertion of a high permeability or permittivity material in a cavity will cause the field distribution to shift. If that material is also lossy (high magnetic or dielectric loss tangent) then the energy will also be attenuated, thus leading to lowering the quality factor of the resonator.

Determining the actual field solutions and excitation mode for a particular component in a cavity might not be practical for cavity with complex geometry. Cutting and pasting absorber pieces in various places on the circuit board cover and testing circuit performance has been the most common method of choosing the best solution. Numerical simulation will be used in this work to determine effective application of absorbing material to mitigating cavity resonance.

1.4 Finite-Difference Time-Domain (FDTD) Simulation of Maxwell Equations

The function of the Finite Difference Time Domain (FDTD) code is to solve Maxwell's equations, commonly seen in differential form:

$$\nabla \times E = -\frac{\partial B}{\partial t} \tag{1.1}$$

$$\nabla \times H = \frac{\partial D}{\partial t} + J \tag{1.2}$$

$$\nabla \bullet D = \rho \tag{1.3}$$

$$\nabla \bullet B = 0 \tag{1.4}$$
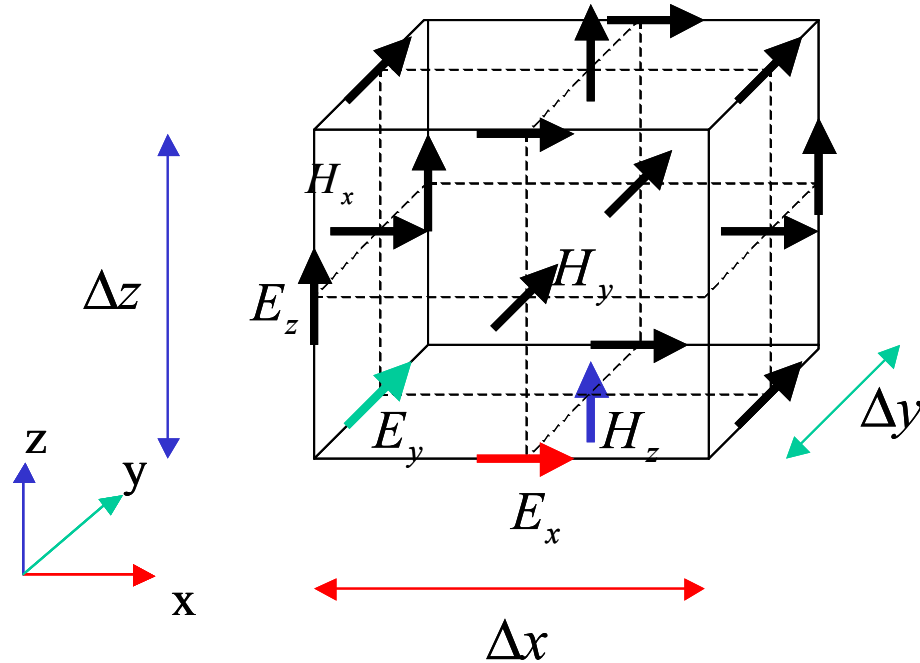
Figure 1.1 Three-Dimensional Yee cell in FDTD

The FDTD method provides a direct equation of Maxwell's time dependent equations. FDTD method has gained prominence among numerical method primarily because of its simplicity. The distinct feature of the FDTD method, in comparison to the Method of Moment (MoM) and Finite Element Method (FEM) is that it is time domain technique. One simulation in time domain results in a solution that gives the response of the system to a wide range of frequencies. By using Fourier transform techniques, the time domain solution can be decomposed into it s spectral component.

The FDTD method is a volume-based method requiring the space of solution be divided into a uniform mesh composed of cells called Yee cell (Fig. 1.1). The E and H field on Yee cell are staggered one half space–cell apart, which facilitates differencing. Leapfrog in time method is applied to the equation, updating each field components for every particular instant of time. Those data of each component at

every time step are stored for further process. This process is illustrated in the following flow chart (Fig. 1.2).

The basics of 3-D Finite-Difference Time-Domain (FDTD) are introduced in this chapter. Based on these knowledge I developed two-dimensional FDTD code in chapter 6 since the underlying principles are the same. A commercial FDTD software tool is used to do the cavity and aperture simulation, which does not require the user to know the theory. However, the fundamental knowledge will help to judge the validity of the simulation and interpret the data.

```
          ┌──────────────────────┐
          │  Calculate E         │
          │  over entire grid     │
          └──────────────────────┘
          ┌──────────────────────┐
          │  Enforce ABC on E     │
          │  at terminal boundary │
          │  and other PEC        │
          │  boundary conditions  │
          └──────────────────────┘
          ┌──────────────────────┐
          │  Advanced time        │
          │  by Δt/2              │
          └──────────────────────┘
          ┌──────────────────────┐
          │  Calculate H          │
          │  over entire grid     │
          └──────────────────────┘
```
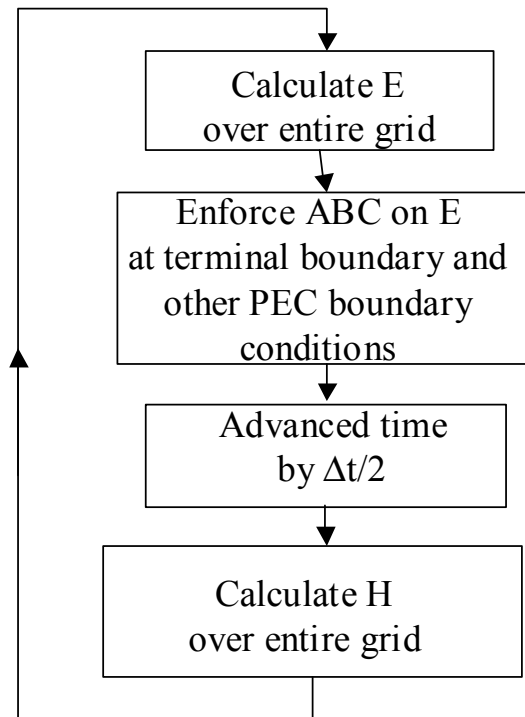
Figure 1.2 FDTD flow chart

Because the FDTD method is time-domain technique, the time iteration must conform to causality principles implying that one advance from one node to the next, in any direction, does not exceed the speed of light. It can be shown that this physical

constraint has a limiting effect on the relationship between the spatial steps $\Delta x, \Delta y, \Delta z,$ and time step Δt. This constrain depends on the FDTD cell size and is given as

$$\Delta t < \frac{1}{\sqrt{1/(\Delta x)^2 + 1/(\Delta y)^2 + 1/(\Delta z)^2}} \tag{1.5}$$

The FDTD requires descretization of the entire domain over which the solution is to be computed. For problems where radiation takes place in an open region, as is the case in the largest percentage of EMI/EMC problem, the domain of the solution fills the entire space and is infinite in extent. However, the mesh has to be truncated to finite size that can be manipulated with finite computer memory. A mesh truncation formulation must be enforced in the outer boundaries of the computational domain to simulate the open region problem. Such mesh termination boundaries must be as non-reflective as possible, mimicking the behavior of free space.

The computational domain size is directly proportional to the memory requirements, and because of this, it is advantageous to keep the boundaries which terminate the computational domain as close to the radiating structure as possible. A poor mesh truncation technique can render the FDTD simulation useless, emphasizing that the quality of the FDTD analysis is highly dependent on the quality of the mesh truncation technique employed.

In the FDTD software used to simulate electromagnetic model, Absorbing Boundary Condition (ABC) is deployed. ABC is mathematical construction taking the form of differential operators that approximates the behavior of outgoing wave.

1.5   Signal Processing

Time domain simulation tools require the transform from time domain to frequency domain if we are concerned the spectral performance. The DFT (Discrete Fourier Transform) make the transformation based on the discrete data result from time domain simulation tool.

Before we get started on the DFT, let's look for a moment at the Fourier transform (FT) and explain why we are not talking about it instead. The Fourier transform of a continuous-time signal $x(t)$ may be defined as

$$X(\omega) = \int_{-\infty}^{\infty} x(t)e^{-j\omega t}\,dt, \qquad \omega \in (-\infty, \infty) \qquad (1.6)$$

The DFT, on the other hand, replaces the infinite integral with a finite sum:

$$X(\omega_k) = \sum x(t_n)e^{-j\omega_k t_n}, \qquad k = 0, 1, 2, ...N-1 \qquad (1.7)$$

Where the variable is defined as:

$x(t_n) = \text{input signal amplitude at time } t_n$
$t_n = nT$
$X(\omega_k) = \text{spectrum at frequency } \omega_k$
$\omega_k = \dfrac{2\pi k}{NT}$
$N = \text{number of time samples} = \text{number of frequency samples}$
$T = \text{sampling interval}$

Calculus is not needed to define the DFT (or its inverse, as we will see), and with finite summation limits, we cannot encounter difficulties with infinities (provided $x(t_n)$ is finite, which is always true in practice). Moreover, in the field of

digital signal processing, signals and spectra are processed only in sampled form, so that the DFT is what we really need.

In the signal processing literature, it is common to write the DFT in the more pure form below:

$$X(k) = \sum_{n=0}^{N-1} x(n)e^{-j2\pi nk/N}, \quad k = 0,1,2,\cdots,N-1 \tag{1.8}$$

$$x(n) = \frac{1}{N}\sum_{n=0}^{N-1} X(k)e^{j2\pi nk/N}, \quad k = 0,1,2,\cdots,N-1 \tag{1.9}$$

where *x(n)* denotes the input signal at time *n*, and *X(k)* denotes the *k*th spectral sample. This form is the simpler mathematically than the previous form that is directly related to physical interpretation.

Chapter 2 Calculation of S-parameters from Time-Domain Algorithms

Linear or nonlinear networks can be characterized by the S-parameters measured at the network terminals. Once the S-parameters of a network have been determined, its behavior to any external stimulus can be predicted under the assumption that the stimulus comes from any of the ports. S-parameters are important in microwave design because they are easier to measure and work with at high frequencies than other type of parameters. They are conceptually simple, analytically convenient, and capable of providing insight into a measurement or design problem.

Measuring most other parameters calls for the input and output of the device to be successively opened and short-circuited. This can be hard to do, especially at RF frequencies where lead inductance and capacitance make short and open circuits difficult to obtain. S-parameters are usually measured with the device imbedded between a 50 Ω load and source, and there is very little chance for oscillations to occur. The cavity for study in this work may not have ports by its structure, so ports will be built for the convenience of S-parameters measurement.

Although a network may have any number of ports, network parameters can be explained most easily by considering a network with only two ports, an input port and an output port, like the network shown in Figure 2.1. Let us assume that we have two ports on a device, a feed port and a receive port, and then the S_{21} parameter represents the forward transmission from the feed port to the receiver port.

The S-parameters describe the interrelationship of a set of variables (a_i, b_i). The variables are complex waves incident on and reflected from the ith port of the network. If V_1 and V_2 are the voltage of port1 and port2 respectively; I_1 and I_2 will be the corresponding current in the port. The normalized incident voltage a_1 and a_2 and normalized reflected voltage b_1 and b_2 (Fig. 1.3) are defined in equation 2.1 – 2.4, where the Z_0 is the characteristic impedance of the ports.
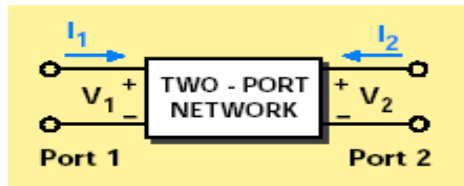
Figure 2.1 Two-port network with voltage and current measurement
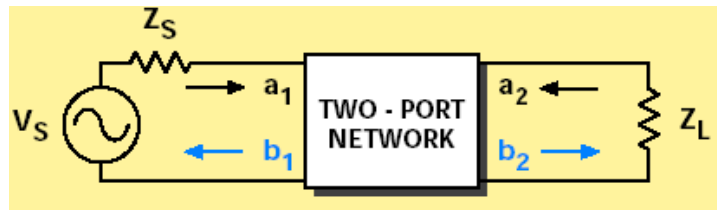
Figure 2.2 Two port network showing incident waves (a1, a2) and reflected waves (b1, b2)

$$a_1 = \frac{V_1 + I_1 Z_0}{2\sqrt{Z_0}} \qquad (2.1)$$

$$a_2 = \frac{V_2 + I_2 Z_0}{2\sqrt{Z_0}} \qquad (2.2)$$

$$b_1 = \frac{V_1 - I_1 Z_0}{2\sqrt{Z_0}} \qquad (2.3)$$

$$b_2 = \frac{V_2 - I_2 Z_0}{2\sqrt{Z_0}} \qquad (2.4)$$

The s-parameters are defined:

$$b_1 = S_{11}a_1 + S_{12}a_2 \qquad (2.5)$$

$$b_2 = S_{21}a_1 + S_{22}a_2 \qquad (2.6)$$

Or explicitly as:

$$S_{11} = \left.\frac{b_1}{a_1}\right|_{a_2 = 0} \qquad (2.7)$$

$$S_{21} = \left.\frac{b_2}{a_1}\right|_{a_2 = 0} \qquad (2.8)$$

$$S_{12} = \left.\frac{b_1}{a_2}\right|_{a_1 = 0} \qquad (2.9)$$

$$S_{22} = \left.\frac{b_2}{a_2}\right|_{a_1 = 0} \qquad (2.10)$$

2.1 Calculation of S-Parameters through Matched Termination

The matched termination will incur no reflection or little reflection at the end of transmission line. This situation helps to derive the S-parameter directly by distinguishing the direction of the traveling wave. Two methods of matched transmission line will be introduced: lumped resistor termination and absorbing boundary condition termination in numerical simulation tool.

2.1.1 Lumped Resistor as Matched Termination

If the load impedance or termination impedance of the transmission line is equal to the characteristic impedance of the transmission line, then this transmission

line has a matched termination. The reflection from the termination is zero according to voltage reflection coefficient equation (2.11) where Z_L is termination impedance and Z_0 is characteristic impedance of the transmission line.

$$\Gamma = \frac{Z_L - Z_0}{Z_L + Z_0} \tag{2.11}$$

Although matched termination is not required to calculate S-parameters, matched termination will make it easier to obtain S-parameter by numerical method as well as instrumental measurement. Since the incident wave reflected from the port termination is zero with matched load, the condition of a_n equals zero in the equation 2.7-2.10 is satisfied. Besides the advantage of this zero incoming wave condition, the outgoing wave b_n is easier to capture because of the absence of incoming wave.
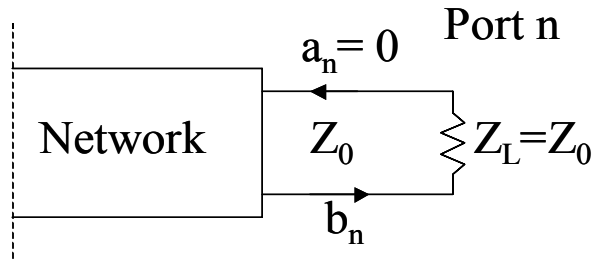
Figure 2.3 Matched termination with zero reflection

The general 50 Ω characteristic impedance transmission line needs a lumped resistor of the same value to be the matched termination as seen in Figure 2.3. The termination of a stripline shown in Fig. 2.4 needs a resistor with the same impedance as the dual line transmission line.
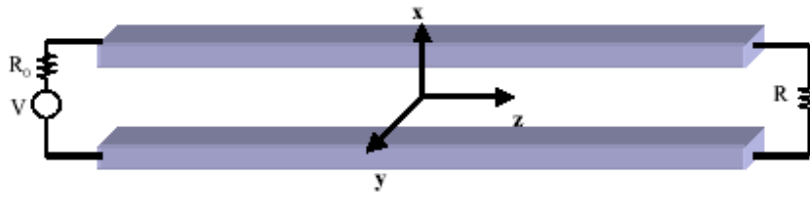
Figure 2.4 Dual line transmission line terminated by resistor

Microstrip and stripline are widely used routing structure in printed circuit board. Other application with geometry different from parallel plane structure may need a coaxial transmitting and receiving port. Coaxial cable consists of an outer conductor layer and a core conductor wire. The closed structure of coaxial cable reduces the interference of electromagnetic wave from unwanted source. Coaxial cable could be connected to a cavity where the inner wire of coaxial is not connecting to the structure, as well as the two-plane geometry where the inner wire has to be physically connected to one of the plane.
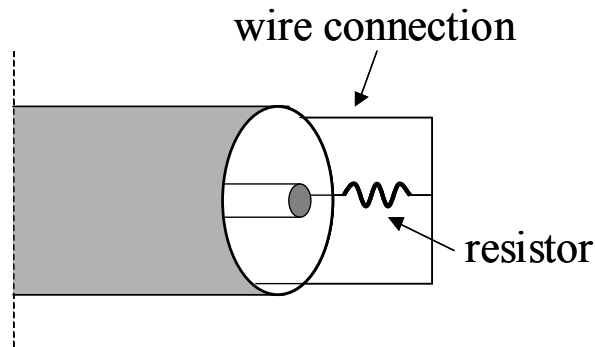
Figure 2.5 Coaxial transmission line with resistor termination

2.1.2 Absorbing Boundary Conditions as Matched Termination

Different from the physical resistor termination for transmission line, the numerical simulation needs an algorithm to implement a virtual matched termination. Absorbing boundary conditions employed in the numerical tool can work as a termination to implement the non-reflection condition.

An open region for unbounded domain is often necessary for the numerical simulation. A suitable boundary on the outer perimeter is needed in this situation to simulate the extension to infinity. Such boundary condition will permit all outward going waves to exit domain as if the computation domain is infinitely large. The absorbing boundary must suppress the reflection,

Several analytical absorbing boundary techniques were invented to annihilate the reflection by applying differential equations based different theory to the outward going waves. Except for the analytical absorbing boundary conditions, perfectly matched layer (PML) is an alternative approach to realize absorbing boundary. It is analogous to the physical treatment of the wall of an anechoic chamber which is highly absorbing in a wide frequency range.

The matched termination could be implemented by applying absorbing boundary at the end of transmission line. The absorbing boundary suppresses the reflection to acceptable level that keeps the time domain solution valid for all time-steps. No matter what kind of boundary condition is implemented to terminate a transmission line, the reflection is not absolutely zero, hence the error for s-parameter need to be considered.

Since the absorbing boundary may work better for normally incident waves, the transmission line terminated by absorbing boundary need to be normal to the absorbing boundary as shown in Fig. 2.6.

transmission line

absorbing condition
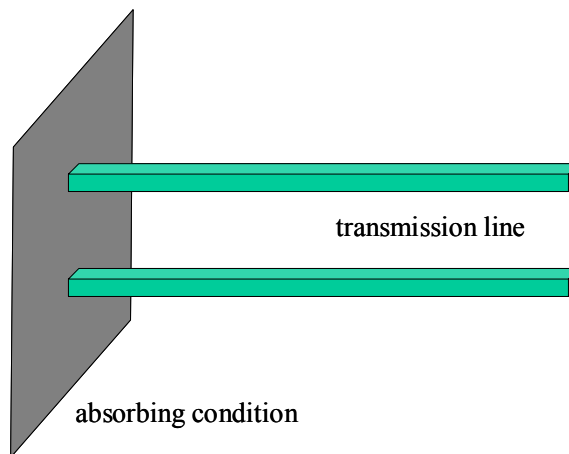
Figure 2.6 Example of transmission line terminated to absorbing boundary with normal angle

2.2   Calculation of S-Parameters through Non-matched Termination

Perfect matching using absorbing boundary conditions is hard to realize in numerical methods. Sometime the reflection is very large that the s-parameter calculation by the assumption of perfect matched termination will no longer be acceptable. This is especially the case when the transmission line is filled with a dielectric material. Therefore, it is necessary to develop a method for S-parameter calculation irrespective of how the transmission line is terminated. The method presented here will be suitable for situations where the reflection from the transmission line termination is unknown or there is considerable amount of reflection from the termination of the port as shown in the Fig. 2.7.

16
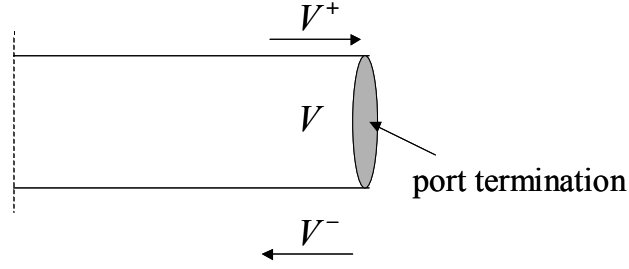
Figure 2.7 Port without considerable reflection

Equations 2.5-2.8 calculate the S-parameter directly under condition of matched termination. If the termination is not matched, it is not possible to tell the incident from the reflected wave in the numerical algorithm. However, the voltage and current of the port is easily available in numerical simulation tools. That information leads to the consideration of S-parameters or Y-parameter. Z-parameters, for instance, are a set of parameters that completely describe the network in a manner similar to how S-parameters describe the same network. Z-parameters are related to voltage and current in a two-port network by the following equations:

$$V_1 = I_1 Z_{11} + I_2 Z_{12} \tag{2.12}$$

$$V_2 = I_1 Z_{12} + I_2 Z_{22} \tag{2.13}$$

Z-parameter and S-parameter are not mutually independent. Assuming the characteristic impedance of all ports is Z_0, Z-parameter and S-parameters are related to each other by equations (2.14)-(2.21):

S-parameters in terms of Z-parameters:

$$s_{11} = \frac{(Z_{11} - Z_0)(Z_{22} + Z_0) - Z_{12}Z_{21}}{(Z_{11} + Z_0)(Z_{22} + Z_0) - Z_{12}Z_{21}} \tag{2.14}$$

$$s_{12} = \frac{2Z_{12}Z_0}{(Z_{11} + Z_0)(Z_{22} + Z_0) - Z_{12}Z_{21}} \tag{2.15}$$

$$s_{21} = \frac{2Z_{21}Z_0}{(Z_{11} + Z_0)(Z_{22} + Z_0) - Z_{12}Z_{21}}$$ (2.16)

$$s_{22} = \frac{(Z_{11} + Z_0)(Z_{22} - Z_0) - Z_{12}Z_{21}}{(Z_{11} + Z_0)(Z_{22} + Z_0) - Z_{12}Z_{21}}$$ (2.17)

Z-parameters in terms of S-parameters:

$$Z_{11} / Z_0 = \frac{(1 + s_{11})(1 - s_{22}) + s_{12}s_{21}}{(1 - s_{11})(1 - s_{22}) - s_{12}s_{21}}$$ (2.18)

$$Z_{12} / Z_0 = \frac{2s_{12}}{(1 - s_{11})(1 - s_{22}) - s_{12}s_{21}}$$ (2.19)

$$Z_{21} / Z_0 = \frac{2s_{21}}{(1 - s_{11})(1 - s_{22}) - s_{12}s_{21}}$$ (2.20)

$$Z_{22} / Z_0 = \frac{(1 + s_{22})(1 - s_{11}) + s_{12}s_{21}}{(1 - s_{11})(1 - s_{22}) - s_{12}s_{21}}$$ (2.21)

If we can solve for the Z-parameters by port voltage and current data, the S-parameter can be calculated from Z-parameter by equation (2.14)-(2.17).

To develop this method, a simple network with only two ports will be considered as an example. Equation (2.12) and (2.13) give us two linear equations with four unknown Z-parameters to describe a two-port network. The Z-parameter will not change with respect to V and I since they are the characteristics of the network. If we have four equations instead of two equations, the four Z-parameters can be solved from the four linear equations. In addition to the two linear equations (2.12) and (2.13), we need another two equations to compose the four equations. To implement this, we may change the initial condition of the numerical simulation; hence V_i and I_i of the network will change correspondingly. The procedure is to run the simulation twice, once with excitation in port 1 and second run with excitation in

port 2. The equations are shown below to describe the two simulations run where V'
and I' denote the value in the second run:

$$V_1 = I_1 Z_{11} + I_2 Z_{12} \tag{2.22}$$

$$V_2 = I_1 Z_{12} + I_2 Z_{22} \tag{2.23}$$

$$V_1' = I_1' Z_{11} + I_2' Z_{12} \tag{2.24}$$

$$V_2' = I_1' Z_{12} + I_2' Z_{22} \tag{2.25}$$

The Z-parameters are solved below from equations (2.26)- (2.29).

$$Z_{11} = \frac{V_1' I_2 - V_1 I_2'}{I_1' I_2 - I_1 I_2'} \tag{2.26}$$

$$Z_{12} = \frac{V_1' I_1 - V_1 I_1'}{I_2' I_1 - I_2 I_1'} \tag{2.27}$$

$$Z_{21} = \frac{V_2' I_2 - V_2 I_2'}{I_1' I_2 - I_1 I_2'} \tag{2.28}$$

$$Z_{22} = \frac{V_2' I_1 - V_2 I_1'}{I_2' I_1 - I_2 I_1'} \tag{2.29}$$

The above equations describe the two-port network Z-parameters
simplification. Then S-parameters can be calculated according to equation 2.14-2.17
given Z_0. This method could be applied to a network with port number larger than
two. However, applying this method to an n-port network requires n times simulation
and solving n^2 linear equations. Even though by the symmetry of a linear network that
$Z_{ij}=Z_{ji}$, the number of equations need to solved is n(n+1)/2. This method may not be
cost efficient for network with large number of ports.

2.3 Calculation of S-Parameters by Modeling the Transmission Line as a Lumped Load

The transmission line may be simplified to reduce the size of the numerical model and therefore save the cost of numerical simulation. The previous two methods mentioned in this chapter do not change the port structure in nature. The first method uses matched termination to obtain incoming or outgoing wave. The second method calculated the S-parameters from Z-parameters regardless of direction of the traveling wave. The third method introduced here will change the structure of the transmission line.

If the port and the network share the same structure such as the microstrip model in Fig. 2.8, the characteristic impedance of the port is that of the structure. The length of the microstrip port will not change the S-parameter calculation as long as the port has a matched termination. Since the numerical model can only have limited dimension in numerical model, we need to implement the effect of infinite structure. One method is to put a lumped resistor of Z_0 impedance between microstrip and the underlying substrate as introduced in previously. The other alternative is to terminate the microstrip and the underlying substrate with absorbing boundary condition as discussed in the section 2.1.

With matched termination, we can shrink the length of the port to a small number. In the case of such consistent structure, the simplification is easy to understand. The next part of this section will introduce the coaxial line port connected to a different structure.

microstrip transmission line
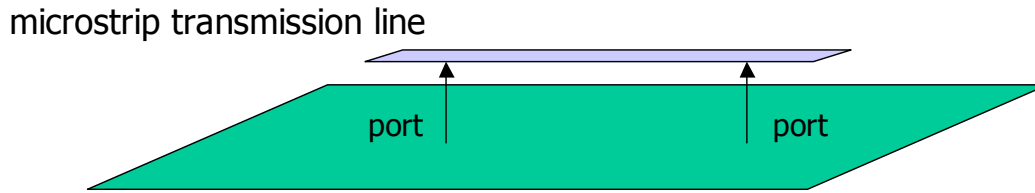
Figure 2.8 Microstrip transmission line with two ports

To characterize the S-parameters of a cavity, a probe is extended into the cavity to capture the field. The voltage induced on the probe is then transferred to the measuring instrument by a coaxial line. The port of the characteristic impedance has to be considered because of the discontinuity between the coaxial cable and the connected network structure.

We can terminate this coaxial line by a resistor of the same impedance as the characteristic impedance of the coaxial line. The resistor connects the surrounding outer conductor and inner wire of the coaxial line. This can be achieved by using one resistor or multiple resistors in parallel to have the same total resistance. One simple method is to close the end of the coaxial line and add a Z_0 resistor of between the outer conductor and inner wire as Fig 2.9 shows.

The idea of shortening the length of the coaxial line is intended primarily to save the computational space. In order to make the numerical model smaller, we can also shrink the length of the coaxial transmission line by pushing the end of the coaxial line to the network structure. Figure 2.9- 2.11 shows the process of shrinking the length of coaxial transmission line as the port of a network structure. As figure 2.10 shows, the coaxial is shortened to some extent compared with figure 2.9. The coaxial can be shrunk further more until finally the length of the coaxial reaches zero

and the coaxial line becomes a lumped resistor inside of the cavity as shown in figure

2.11.
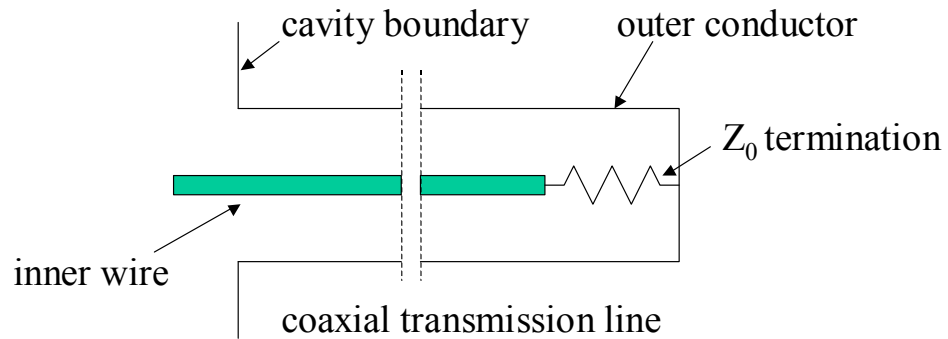
Figure 2.9 Coaxial cable transmission line with Z_0 termination
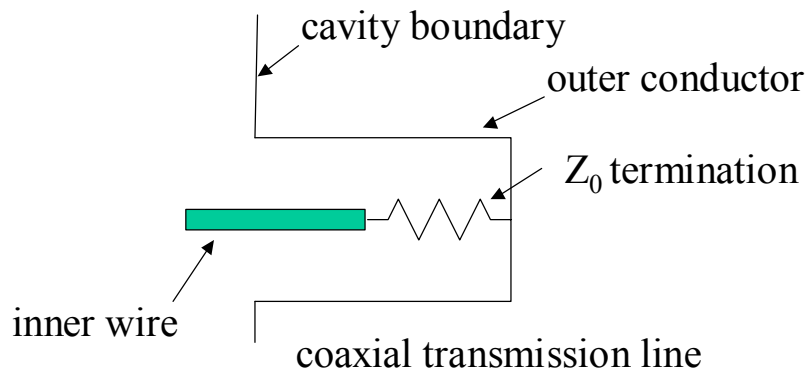
Figure 2.10 Coaxial line terminated with a lumped resistor with shortened length
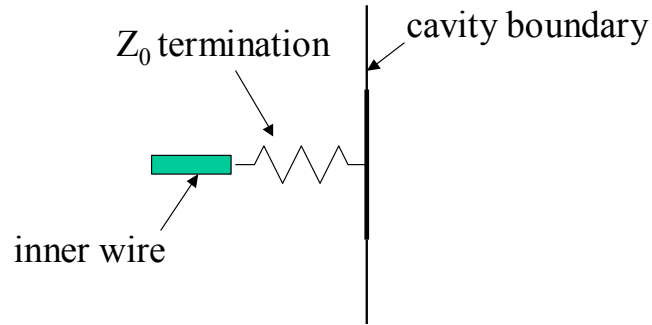
Figure 2.11 Zero length coaxial line represented by a lumped resistor

In Fig. 2.11 the outer conductor layer of the coaxial line merges with the conductor boundary of the network structure. The length of inner wire contained in the cavity remains the same, considering the size of the resistor is electrically very small. This simplification ignores the reflection by the discontinuity where the port and network structure is joined. This simplification is very important to calculate the S-parameters of coaxial port connected to a cavity.

In this chapter, three methods were introduced to facilitate the calculation of S-parameters from time-domain electromagnetic numerical simulation. The effectiveness of these methods will be discussed in next chapter by applying a rectangular enclosure with two coaxial ports. The experiment measurement and numerical calculation of S-parameter using the three methods will be compared.

Chapter 3 Cavity Resonance Characterization and Mitigation

An electromagnetic radiation source, such as the heat sink of a high-speed microprocessor, when placed in an enclosure or chassis, leads to cavity resonance that can have severe impact on other electronic components housed within the same enclosure. The cavity resonance can also potentially affect external radiation caused by apertures present on the body of the enclosure [19]. As an example, Fig. 3.1 shows that the radiation through an 20×2mm aperture present in a infinitely large shielding plate and the radiation through the same aperture when backed with a rectangular cavity of size 60×32×70mm. The magnitude of electric field through the cavity backed aperture is observed to be much higher within specific frequency ranges because the electric field inside enclosure is strengthened by cavity resonance. Reducing the enclosure resonance is a critical step in the overall improvement of the electromagnetic compatibility performance of enclosures.

The S-parameters are employed to characterize the resonance of the enclosure. For a two-port network whose model is described in Fig. 2.1 and Fig. 2.2, S_{21} describe the transmission from port 1 to port 2. If the resonance occurs at certain frequency where energy is built up, the energy will transmit to port 2. Similar explanation can be applied to the S_{11} which is the reflection coefficient of port 1. If the energy can be built up in a device at certain frequency, the device will reflect little energy. So a very small S_{11} is indicative of resonance.

The methods described above for calculation of the S-parameters will be applied to characterize highly resonant cavity structures that is commonly used to house high-speed electronic components. By using novel material and certain configuration, the resonance of these cavities can be mitigated. However, experimenting with prototypes can be highly costly, and more critically, time consuming. The proposed numerical procedure for S-parameters calculation incorporates the Finite-Difference Time-Domain (FDTD) method.
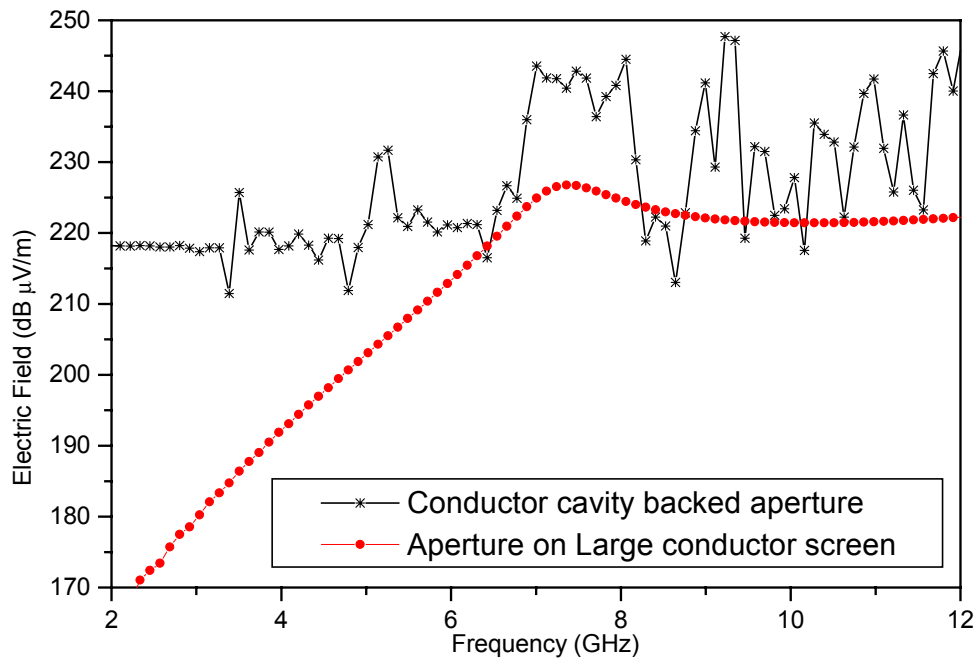
Figure 3.1 Radiation through aperture on large plate and aperture on a cavity

The S-parameter calculated by numerical method will be compared to the experimental measurement. S-parameter measurement can be easily implemented in the laboratory using a vector network analyzer (VNA). In this work, Agilent E8364A

VNA (Fig. 3.2) working in 45MHz-50GHz frequency range was used for all measurements.

Figure 3.2 Agilent E8364A Network Analyzer 45MHz-50GHz

Analytical solutions are available to characterize the resonance of simple enclosures such as a parallelepiped shown in Fig. 3.3, or canonical cavities.
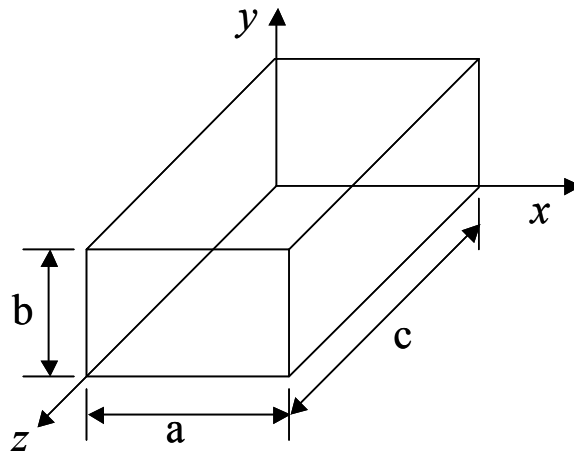
Figure 3.3 Rectangular cavity

For the cavity shown in Fig. 3.3, the resonant frequency is given by

$$f_r = \frac{1}{2\pi\sqrt{\mu\varepsilon}} \sqrt{\left(\frac{m\pi}{a}\right)^2 + \left(\frac{n\pi}{b}\right)^2 + \left(\frac{p\pi}{c}\right)^2} \qquad (3.1)$$

where integer *m, n, p* is the index of the resonance modes.

Adding absorbing material is a widely used method to reduce resonance in cavities. Numerical methods are capable of modeling complex structure and material properties, for which analytical methods do not work. Numerical simulation can lead to significant cost savings by reducing physical prototyping. The result of numerical modeling will give confidence of how the absorbing material works. Numerical simulation can also lead to material saving as optimization techniques can be employed to select minimal material usage that achieves desired objectives.

3.1   Numerical Model and Procedure

To validate our numerical procedure, a stainless steel box with SMA connector as output port measuring 15 cm x 25 cm x 30 cm (see Fig. 3.3) was constructed. The resonant frequencies for this structure were obtained experimentally through the S-parameter measurements using a vector network analyzer. The experiment measurement is the benchmark to evaluate FDTD simulation because of its high level of accuracy. The data process is critical in FDTD calculation of S-parameter, since direct data of S-parameter is unavailable in FDTD simulation. Three numerical procedures developed in chapter 2 to calculate S_{21} parameter will be implemented here. The numerical simulations results and experimental measurements will be compared.

Figure 3.4 Stainless steel enclosure (cavity) with SMA connectors at the port locations.

Fig. 3.5 shows the profile of the numerical model of conducting enclosure with feed and receiver ports at exactly where the physical ports are located. There are two SMA connectors on the stainless steel enclosure as the two ports connected to the network analyzer by two 50-ohm standard coaxial cables. The core wire of coaxial cable in port 1 stretches across the inner space of the enclosure and is terminated by a 50-ohm resistor. This diagonal conductor line enhances the propagation of electromagnetic wave travels in different modes in the rectangular resonant cavity. The core wire of coaxial cable for port 2 extends into the cavity by 10mm.

3.1.1 S-parameters Calculation with Coaxial Cable Terminated by Absorbing Boundary Condition

The first method developed in chapter 2.1 will be implemented here. In the FDTD model, we simulate the coaxial cable connected to port as a rectangular waveguide that has a conductor line at the center. An impressed current source is placed in the middle of port 1 to excite the enclosure. For a two-port network model

in Fig 3.5, the S_{21} parameter is defined in equation (2.8). With application of absorbing boundary conditions, there should be no incoming waves from boundary into the enclosure in port 2, so that $a_2=0$ condition is satisfied.

The total voltage we measured in port 2 equals the outgoing wave voltage b_2 since incoming wave voltage a_2 is zero. The problem is that the voltage a_1 cannot be measured directly since there is reflection from the junction discontinuity of enclosure and port 1, i.e. voltage of outgoing wave b_1 is not zero. This problem is solved by using a separate model of port 1 (Fig. 3.6). Absorbing boundary condition is applied to both ends of port 1, so that the monitor points in the middle of port only collects the voltage of incoming waves a_1 generated by the same source which is the same as the whole enclosure model. After this simulation, the a_1 is measured.
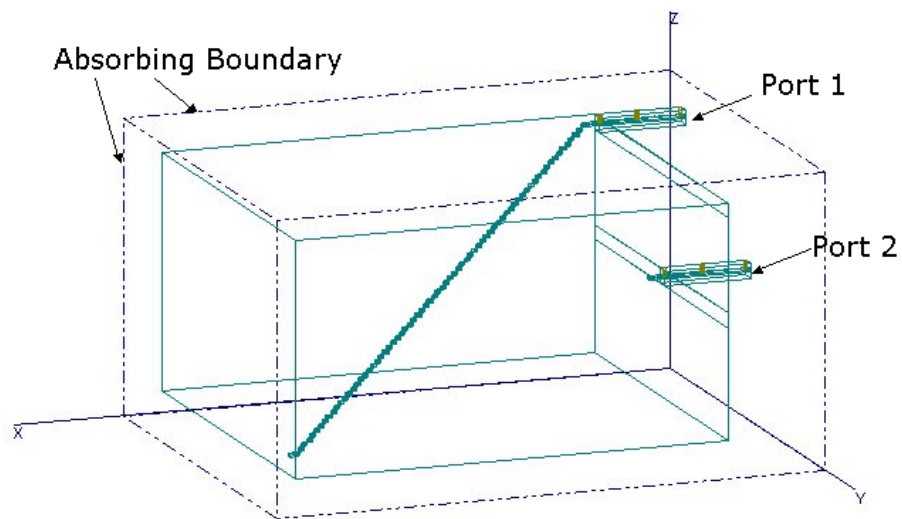
Figure 3.5 FDTD Numerical model of resonant enclosure

29

The time domain voltage data of b_2 and a_1 is processed using Discrete Fourier Transform (DFT) defined by equation 1.8, to obtain the frequency domain behavior. The calculation is implemented by using Matlab.

FDTD method divides the computation space into uniform mesh and iterate the field variable along time steps. The time interval Δt in both the FDTD model of enclosure and separate port need to be the same to facilitate calculation of frequency corresponding to $X(k)$. Both models are run for 60000 time steps to optimize frequency resolution which equals to $(1/\Delta t)$ divided by time steps N.

If the time step N equals to the power of two, the *fft* function in Matlab will apply the Fast Fourier Transform (FFT) algorithm, an efficient method for DFT calculation. While N is not equal to power of two, Fast Fourier Transform will require zeros to be padded to the end of finite sequence of time domain sequence to make N equals to power of two. However, the padded zeros will bring spurious wiggles to the spectrum curve as a result of the convolution process in the frequency domain. In this work, zero padding is not used.

The amplitude of the complex result of DFT on b_2 and a_1 is calculated and then the ratio of the amplitude is converted to dB unit. The numerical result of S-parameter is shown in Fig. 3.7 with experiment measurement as benchmark. The other numerical method to calculate S_{21} will be compared with this result next.
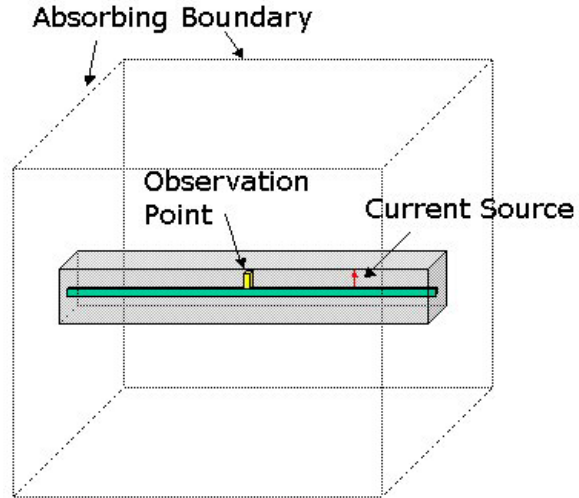
Figure 3.6 Separate model of source input coaxial
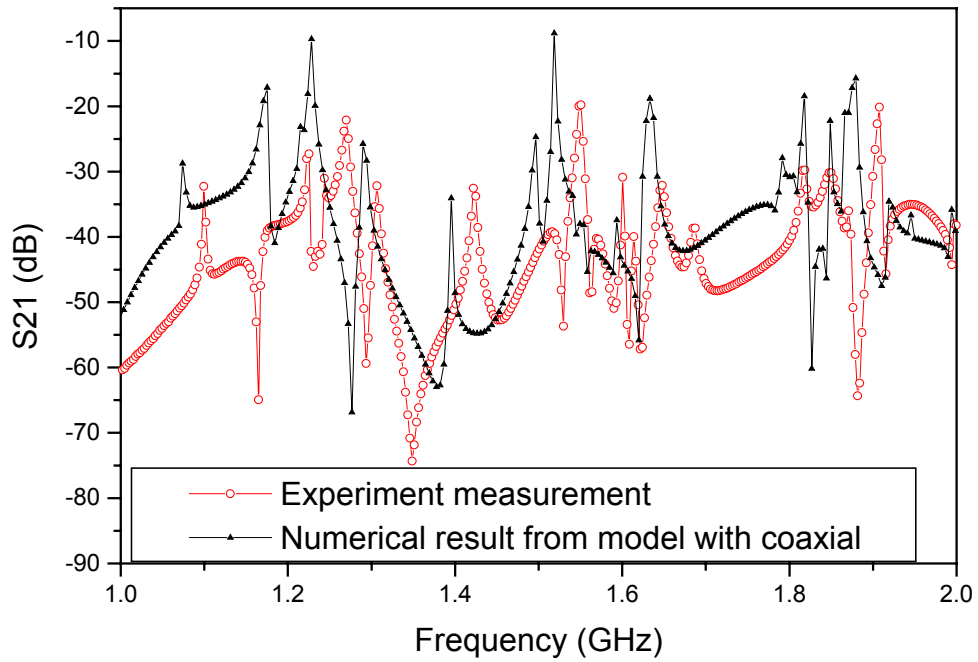
Figure 3.7 S_{21} parameter calculation from cavity model with coaxial cable

31

3.1.2 S-parameters Calculation without Considering Incoming and Outgoing Wave

The method introduced in chapter 2.2 is implemented to extract the S-parameters of the enclosure. The model shown in Fig. 3.5 is used for this simulation. The difference is that the separate model for port 1 is no longer needed. However, we need to run the simulation twice: In the first run, the source is located at port 1; for the second run, the source is located at port 2.

The FDTD captures the voltage and current data in coaxial ports by the voltage and current probes provided by the software. The process consists of two simulations in which the source is located in number 1 and number 2 coaxial cable respectively. All the voltage and current data from the second run is denoted with prime while the first time simulation data without superscription as shown in equation 2.22-2.25.

After applying FDTD data from the two simulation runs to equation 2.26-2.29, the Z parameters are calculated. The Z parameters are then substituted to equation 2.14-2.17 to calculate the S-parameters.

The result of this method is shown in the Fig. 3.8. The frequency of the peaks of S_{21} is more accurate compared with the Fig. 3.7. However, the profile of the amplitude of the S_{21} is higher than experiment test. The reason of the discrepancy may be the ideal condition in numerical simulation that does not incur any dissipation in the perfect conductor surface. Considering the real world energy loss, the experiment S_{21} measurement should be lower than numerical result.
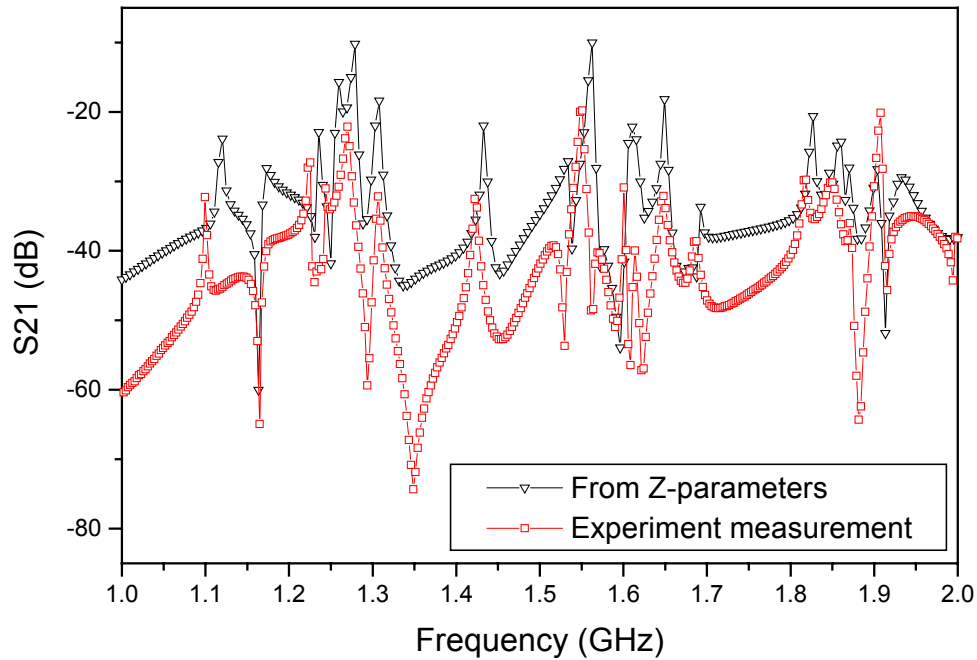
Figure 3.8 S_{21} parameter calculation from numerical method without considering incoming and outgoing wave data

3.1.3 S-parameters Calculation from lumped element simplification model

According to the method introduced in chapter 2.3, 50 ohm coaxial cable is simplified to a lumped resistor. The voltage captured by 50-ohm resistance is considered sum of waves that travel in two directions. So the incoming wave is half of the given voltage source.

The time domain data of the source in port 1 is divided by two before applying Discrete Fourier Transform calculation. The voltage captured by lumped resistor standing for receiving port 2 is considered outgoing wave. The S_{21} is calculated following equation (2.8). The S_{21} result is depicted in Fig. (3.9).

Since FDTD computational model consists of rectangular cubic cells, any curve shape structure must be fitted by staircase cells. The limited size of the coaxial cable model determined that the coaxial has to be modeled as a square waveguide with inner wire. This square waveguide simplification of cylindrical coaxial cable might bring error to simulate the cavity resonance. This might be one of the reasons that lumped element model gives a better solution compared to enclosure with coaxial cable model.
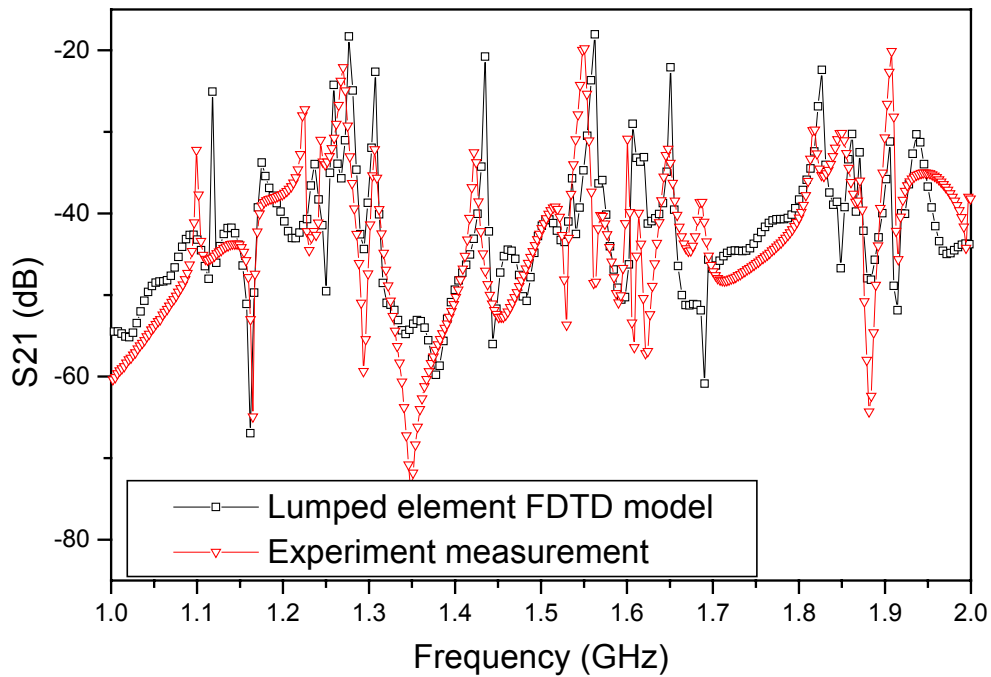
Figure 3.9 Computational result of the resonant cavity S_{21} compared with testing measurement

3.1.4 Comparison of the Three Numerical S-parameters Method

In Fig. 3.9, there is strong correlation between the peaks of the two curves whereas the frequencies of the peaks may not be exactly the same. There are frequency shifts between the peaks of the two curves, i.e., the frequencies of some

34

peaks of the numerical result are a little bit higher than that of experimental measurement.

The overall profile of the numerical result curve agrees well with experiment result. Generally, the magnitude of numerical curve is comparable with the experiment data and the difference varied along the frequency range.

Compared with Fig. 3.7 which has the largest error both in amplitude and resonant frequency, the result of Fig. 3.8 is acceptable. However, none of the result in Fig. 3.7 and Fig. 3.8 is as good as the result in Fig. (3.9). The agreement between numerical result and experiment data validate the lumped element simplification of transmission line as a proper method to implement time domain numerical calculation of S-parameters.

3.2 Cavity Resonance Mitigation Using Lossy Material: Numerical Study

Cavity resonance problems are critical in the design of high-speed circuits. A circuit can be tuned to work properly but when a circuit board housing is used to physically protect the circuit, resonance often arise in the cavities. Resonance can have an adverse effect on performance, or even possibly make the component fail to work.

Resonance absorbers may be thought of as circumventing the problem of high interface reflection by canceling this reflection with another from the back surface. If the back surface is a conductor, it may be shown that these two vectors cancel at a frequency where the medium is essentially a quarter-wave (or odd multiples of a quarter wave) thick. By adjusting the thickness and material property of the medium,

a condition of low reflection is achieved at the resonant frequency for angles near normal incidence.

The objective of this work is not to absorb the energy completely in the cavity, but try to lower the resonance. Thin resonance absorbers are preferred for most applications where the space of the enclosure is limited. They are usually mounted directly on the metal that is causing the reflection since reduction of reflection is expected. The limited reflectivity characteristics of resonant absorbers, especially at wide angles of incidence, lead to the use of the material to lower the quality factor of the resonant structure. The quality factor, Q, of a resonant system is considered to be high if the system loses little energy over time compared to the energy in the system.

Adding microwave absorbing material to a cavity has proven to be a quick and inexpensive way to eliminate cavity resonance. From basic field theory, the insertion of a high permeability/permittivity material in a cavity will cause part of energy to be stored by the material. If that material is also lossy, i.e. having high magnetic or dielectric loss tangent, then the energy will be dissipated.

Following the numerical procedure we introduced above, we will study the resonance characteristic of the enclosure with microwave absorbing material. As an example, we choose the material property to be ε_r=9, σ=0.17 $\Omega^{-1}m^{-1}$. The shape and the location of the absorbing material will play an important role in the overall S_{21} dampening effect which can not be described analytically. However, with the procedure developed in this work, we can test materials with complex shapes and different placement configurations.

Two absorbing material configurations of the material will be studied for their performance. In the first absorbing material configuration, a 2mm thick absorbing sheet measuring 26 x 30cm fully covers the bottom of the enclosure as shown in Fig. 3.10. If the sharp peaks of S_{21} is lowered and flattened, then we can consider the resonance to be mitigated.

The S_{21} parameter is considerably changed by the first absorbing sheet configuration, compared with that of empty enclosure as shown in Fig.3.11. In lower frequency range from 1 GHz to 1.2 GHz, the S_{21} parameter drops about 10 dB and those upward peaks standing for resonance are suppressed. In higher frequency range above 1.2 GHz, the overall magnitude of S_{21} is also lowered with a largely flat profile without notable peaks. The absorbing material sheet achieves considerable resonance mitigation especially explicit in the frequency range of my concern.
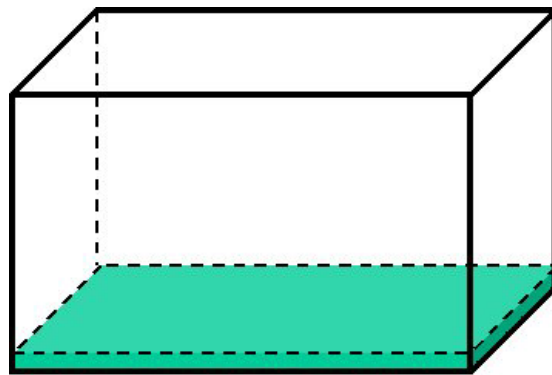
Figure 3.10 Absorbing material sheet on the bottom of enclosure
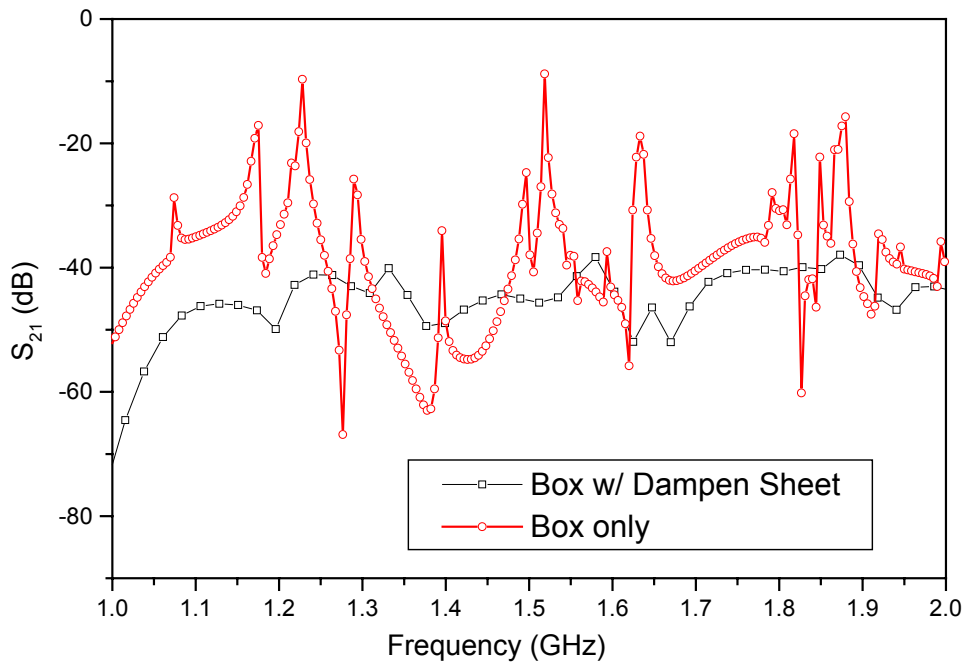
Figure 3.11 S_{21} parameter change with absorbing sheet

In the second configuration, the absorbing sheet is cut to 2cm wide strips, and arranged at intervals of 4cm on the enclosure bottom (Fig. 3.12). The 300 mm long enclosure bottom contains eight 20mm strips and seven 20mm spacing in between them. Eight absorbing strips covers about half of the bottom area, in other words, about half of the absorbing material is saved compared with the absorbing sheet. The performance of these absorbing strips is compared with whole absorbing sheet in Fig. 3.13.
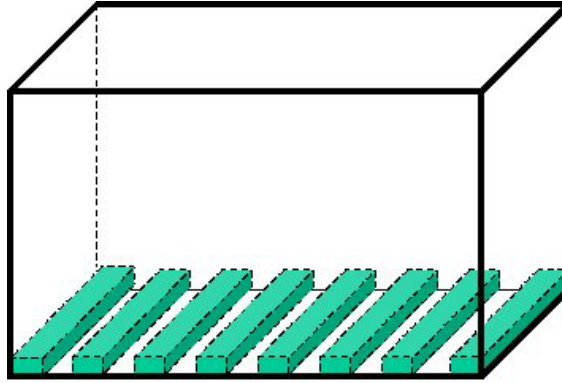
Figure 3.12 Absorbing material strips on the bottom of enclosure

The absorbing strips do not work well in some frequency range such as from 1 GHz to 1.05 GHz and from 1.35 GHz to 1.4 GHz. In the rest of other frequency range, they achieve some extent of resonance mitigation as well although may not be as good as the first sheet configuration. The S_{21} curve of absorbing strips configuration is not as flat as that of absorbing sheet configuration, going up and down around the S_{21} curve of absorbing sheet.

The performance of absorbing strips to mitigate resonance is comparable to the absorbing sheet. Although the amplitude of the S_{21} of strip configuration is a little bit higher than that of whole sheet configuration, there is substantial drop for the two configurations compared with the peaks of no absorbing material model. The desire of resonance mitigation may be well satisfied by the strip configuation. In addition, half of the absorbing material is saved. Using the validated S-parameters calculation, we can try different structure, material geometry and electromagnetic properties with confidence.
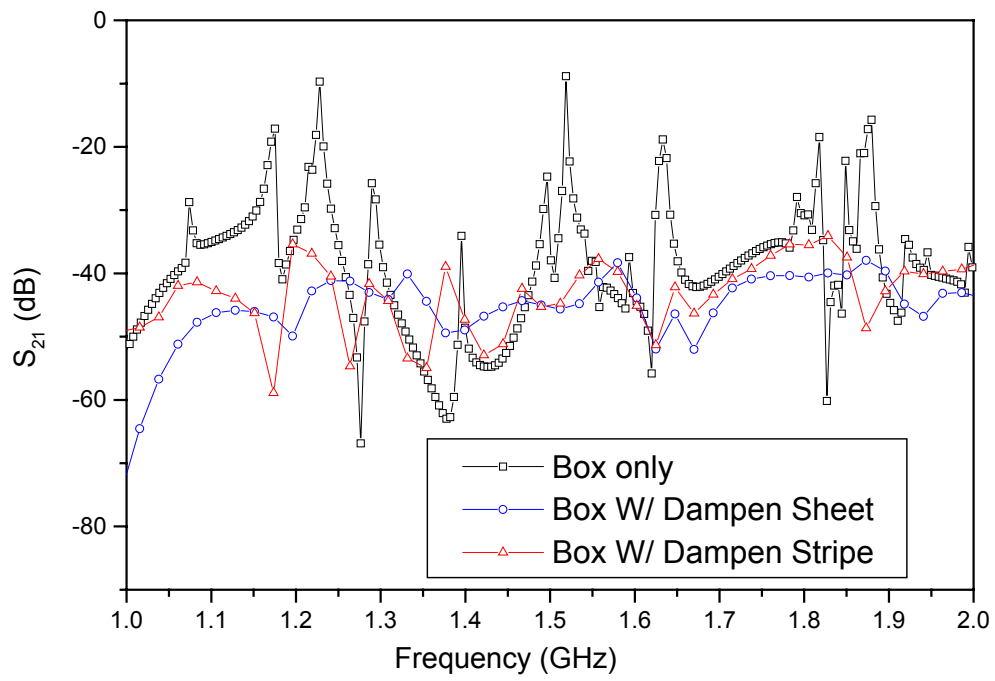
Fig. 3.13 S_{21} parameter Comparison between absorbing sheet and absorbing strips

Chapter 4 Reduction of Radiation from Resonant Apertures

The proliferation of high-speed electronic device and communication equipment brings an increasingly hostile electromagnetic environment. Furthermore, the increase in electronic devices sensitivity due to diminishing tolerance levels is increasing the vulnerability of these devices to external electromagnetic threats. In fact, several governmental and non-governmental research initiatives have been initiated recently to address these critical and important threats to the overall robust operation of electronic equipment in military and civilian settings (see [20] for example). The work presented in this chapter addresses a critical electronic enclosure design parameter that predominates the effectiveness of electronic enclosures to function as shields of electromagnetic energy.

Metallic enclosures are commonly used to reduce emission from electronic devices and boards, and to improve the immunity of the same electronic equipment to external interference and threats. In cases where the frequency is high enough such that the skin depth is less than the thickness of the shield, the overall shielding effectiveness will not be determined by the shield material properties but by the apertures and opening on the shield or chassis. These apertures may be introduced intentionally, as would be the case when airflow is needed for cooling, or unintentionally as the inevitable joint seams of shields or small openings in doors with imperfect gaskets.

To meet electromagnetic compatibility (EMC) and electromagnetic interference (EMI) requirements, it is crucial to quantify the electromagnetic field

penetration through apertures and other chassis openings such as seams and gaskets. The leakage of electromagnetic waves through apertures in enclosures is critical at frequencies where the wavelength approaches the dimension of the aperture.

In this chapter, we focus on the problem of radiation through an aperture in an infinite large conducting plane, thus ignoring any effects induced by the enclosure such as the resonance of the enclosure and complex field interaction with internal structures. This initial focus is intended to develop an understanding for the electric current density distribution in the immediate vicinity of the aperture. Our objective is to gain additional insight into the underlying aperture radiation mechanism and develop techniques to reduce the radiation without affecting the overall see-through size of the aperture.

Ideas previously proposed include changing the configuration of apertures [15], using double perforated screen to lower the radiation leakage [21], and using dielectric to fill the aperture [22]. The technique to lower the radiation through the aperture as well as keep the size and position of the aperture is highly demanded for the commonly seen aperture designed for heat dissipation.

To improve shielding effectiveness due to the presence of an aperture in an infinite metallic screen, we introduce a novel technique that is based on the application of resistive sheets (coating) to the area immediately surrounding the aperture. The primary objective in our technique is to lower the radiation through the aperture while maintaining constant aperture size in order not to affect airflow and heat transfer which is a major consideration for enclosures containing high-speed

electronics. The proposed technique is tested using a commercial numerical analysis tool based on Finite-Difference Time-Domain (FDTD) method.

4.1 Analytic Solution of Radiation from Aperture

The radiation fields from aperture, such as slots, open-ended waveguides, horns, reflector and lens antennas, are determined from the knowledge of the fields over the aperture of the antenna.

The aperture fields become the sources of the radiated fields at large distances. The analytic solution introduced in this chapter is a variation of the Huygens-Fresnel principle, which states that the points on each wavefront become the sources of secondary spherical waves propagating outwards and whose superposition generates the next wavefront [23].
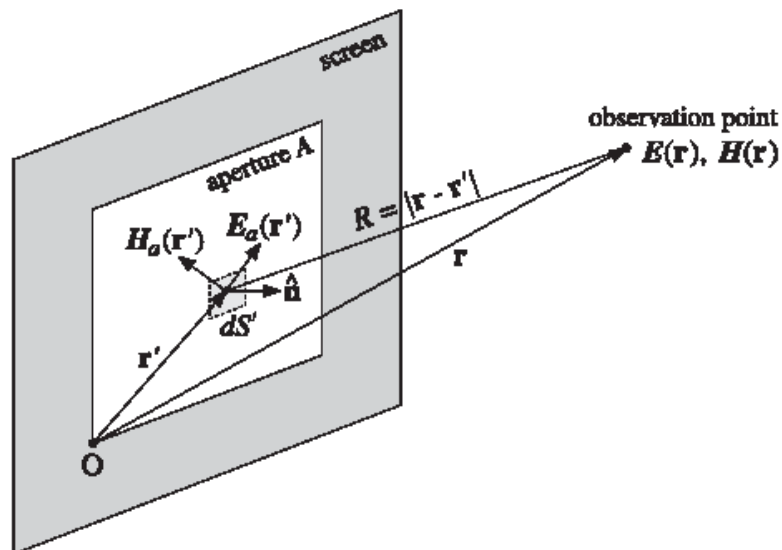
Figure 4.1 Radiated field from aperture

Let E_a, H_a be the tangential fields over an aperture, as shown in Fig. 4.1. These fields are assumed to be known and are produced by the sources to the left of the screen. The radiated fields can be computed with the help of the field equivalence principle, which states that the aperture fields may be replaced by equivalent electric and magnetic surface currents.

The equivalent surface currents are:

$$J_s = \hat{n} \times H_a$$
$$J_{ms} = -\hat{n} \times E_a$$

(4.1)

where $\hat{n}$ is a unit vector normal to the surface and on the side of the radiated fields. Thus, it becomes necessary to consider Maxwell's equations in the presence of magnetic currents and derive the radiation fields from such currents.

The solutions of the Helmholtz equations are given in terms of Green function:

$$G(r - r') = \frac{e^{-jk|r-r'|}}{4\pi|r-r'|}$$

(4.2)

Using the Lorenz conditions, the scalar potentials may be eliminated in favor of the vector potentials, resulting in the following expressions:

$$E = \frac{1}{j\omega\mu\varepsilon}\left[\nabla(\nabla \cdot A) + k^2 A\right] - \frac{1}{\varepsilon}\nabla \times A_m$$
$$H = \frac{1}{j\omega\mu\varepsilon}\left[\nabla(\nabla \cdot A_m) + k^2 A_m\right] + \frac{1}{\mu}\nabla \times A$$

(4.3)

The vector potentials in equation 4.3 are expressed in equation 4.4 where V is the volume over which the charge and current densities are nonzero. The observation point r is taken to be outside this volume.

$$A(r) = \int_v \mu J(r')G(r - r')dV'$$

$$A_m(r) = \int_v \varepsilon J_m(r')G(r - r')dV'$$

$$(4.4)$$

4.2   The Aperture as a Transmission Line

The analytic solution in the previous section is based on the known electric field and magnetic field in aperture that is practically very difficult to measure. The application of numerical tool will be feasible to study the radiation and mitigation technology.

The field mitigation method presented in this work is based on a novel interpretation of the aperture as a transmission line where the power or energy transmission takes place in the plane of the aperture. (This interpretation is drastically different from the works in [4]-[7] where the aperture is considered as a load-discontinuity in a transmission line system composed of the interior cavity and exterior open space.) To motivate this interpretation, we consider an electromagnetic transient wave impinging upon an aperture from one side. The initial part of the transient pulse contains the high-frequency spectrum and is expected to appreciably leak through the aperture. After the initial part of the transient passes through the aperture, one would expect a certain point in time after which some energy starts traveling within the aperture along the directions of the dominant (longer) axis. Naturally, the currents traveling along the edges of the aperture support the field within the aperture. When the field or current reaches the edges of the aperture, it is reflected back. The oscillation of the field (or current) back and forth along the edges

terminating the longer axis of the aperture in essence gives rise to what is typically referred to as aperture resonance.

To illustrate this phenomenon further, let us consider an aperture measuring 2mm x 20mm placed in an infinite perfectly conducting screen as shown in Fig. 4.2. The aperture resonance phenomenon is observed in Fig. 4.3, which shows three snapshots derived from time-domain simulation of a field incident on the same size aperture. These snapshots show a standing-wave pattern of the field within the aperture at different time instances, a behavior that strongly resembles transmission-line type propagation. Now, with this physical perspective, we interpret the long edges of the aperture as forming a transmission line system (along which the propagation takes place) and the short edges as the termination of the transmission line, as shown in Fig. 4.4. One can assume without any loss of generalization that at resonance, the field excitation is positioned at the middle of the aperture. The field excitation is depicted as a voltage source positioned between the two long edges of the aperture as shown in Fig. 4.4. As a consequence to this aperture model, if a suitable matching load were positioned at the two ends of the aperture, one would expect that the outgoing fields, and supporting currents on the conducting surface surrounding the aperture, would be absorbed or reduced considerably. In a conceptual perspective, a matching load in this case would be distributed as depicted in Fig. 4.5. If a suitable termination were used under this interpretation, the source that is positioned at the center of the aperture would be expected to give rise to outgoing waves (outgoing with respect to the source and in the plane of the aperture).
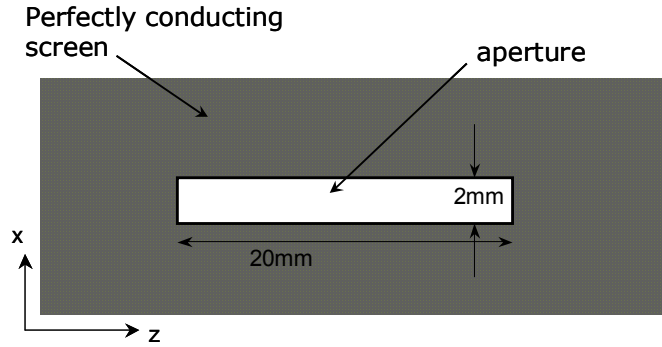
Figure 4.2 An aperture measuring 2mm x 20mm placed in an infinite perfectly conducting screen.
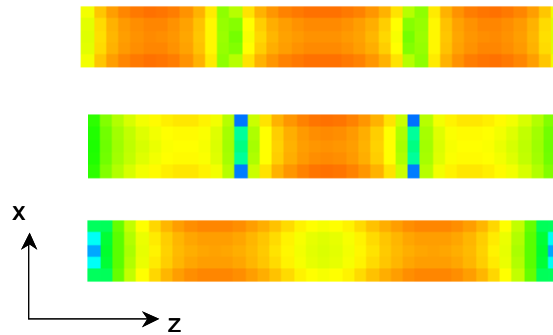
Figure 4.3 Three different snapshots of the field within the aperture. The excitation is a Gaussian pulse impinging on the aperture from one side.
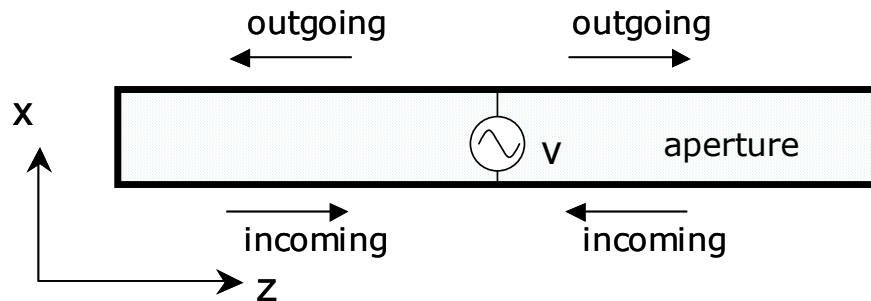
Figure 4.4 Depiction of the transmission line model of the aperture.
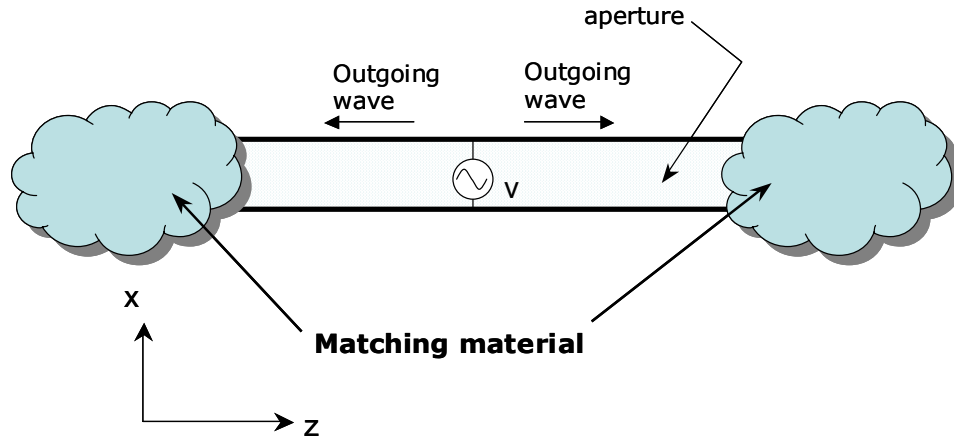
Figure 4.5 Matching material placed at the short edges of the aperture with the intention of absorbing the outgoing waves.

In light of the above interpretation, the techniques proposed in this work are based wholly on the concept of adding a resistive sheet to the immediate surrounding of the aperture in order to provide matching medium for the fields that oscillate within the aperture. This resistive material is intended to act as a matching load that absorbs the outgoing waves, thus considerably reducing resonance. In the following section, we test this concept with the help of the Finite-Difference Time-Domain (FDTD) method.

4.3   Rectangular Loaded Apertures

The term "loaded aperture" will be used in this work to refer to an aperture coated or surrounded by resistive sheets. The resistive sheet concept depicted in Fig. 4.5, can be applied in an infinite number of configurations. In this work, we will confine our investigation to three configurations only. As a starting point, a resistive sheet was applied close to the shorter edges of the aperture as shown in Fig. 4.6. This

configuration will be referred to as Configuration A. Notice that to maintain the same see-through aperture area as before the application of any sheets, the actual metallic screen cutout is enlarged and the resistive sheet is effectively covering part of the aperture. As a second configuration, we placed a resistive sheet in the region surrounding the aperture such that the perimeter of the aperture will be composed of the resistive sheet, as shown in Figs. 4.7 and 4.8. (Again, the actual see-through aperture area is maintained at 2mm x 20mm.) This second configuration will be referred to as Configuration B. In the third configuration, a resistive sheet is placed on top of the conducting screen from both sides of the aperture. This placement resembles a frame-like figure as shown in Figs. 4.9 and 4.10. This third configuration will be referred to as Configuration C. Notice that the area of the aperture (physical opening) remains unchanged in these configurations such that the heat transfer requirements of the shielding plane (screen) remain unaffected. Figure 10 shows a view of the aperture seen from either the interior or exterior side for configurations A and B. The parameter w in the figures designates the width of the resistive sheet.

There are infinite possibilities for the type of material used in the resistive sheets. Our choice for the material will is chosen such the material is either available in the market, or can be fabricated using existing technology. The material parameters for the resistive sheet will be chosen such that $\mu_r = 1$, $4 \leq \varepsilon_r \leq 20$, and $5 \leq \sigma \leq 30$ Ohm^{-1}m^{-1}. We emphasize here that systematic optimization of the resistive sheets material property is outside the scope of this work and is intended for future work. Furthermore, the effect of magnetic sheets is differed to future work.
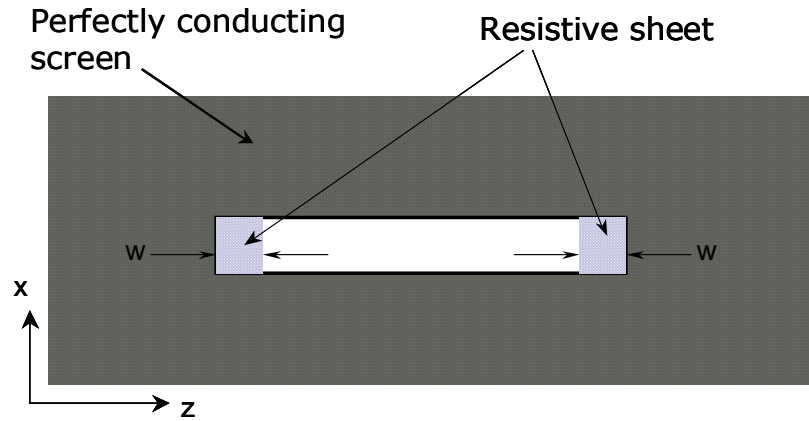
Figure 4.6 Configuration A. Resistive sheets are placed close to the shorter edges of the aperture.
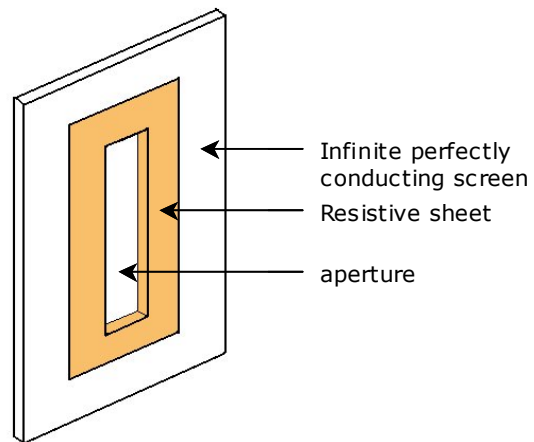
Figure 4.7 Configuration B. The resistive sheets constitute an inner frame that is completely contained within the aperture.
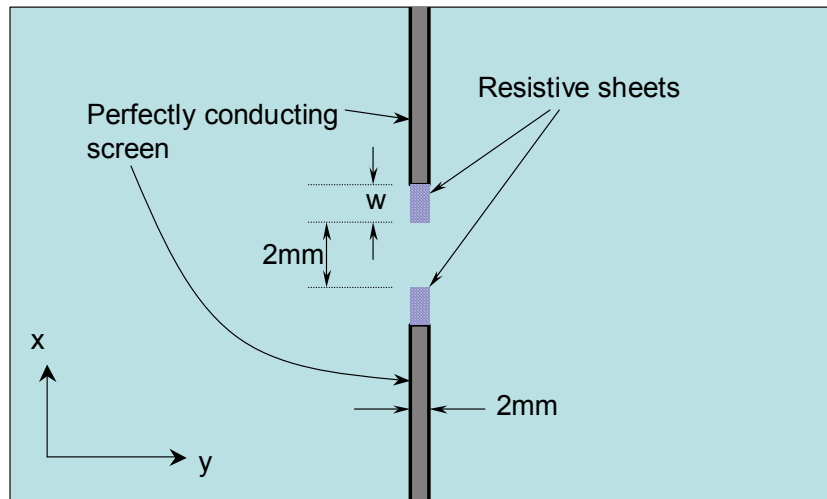
Figure 4.8 Cross section (x-y plane) showing the application of resistive sheets in Configuration B. Notice that the see-through aperture size and area remained unchanged.
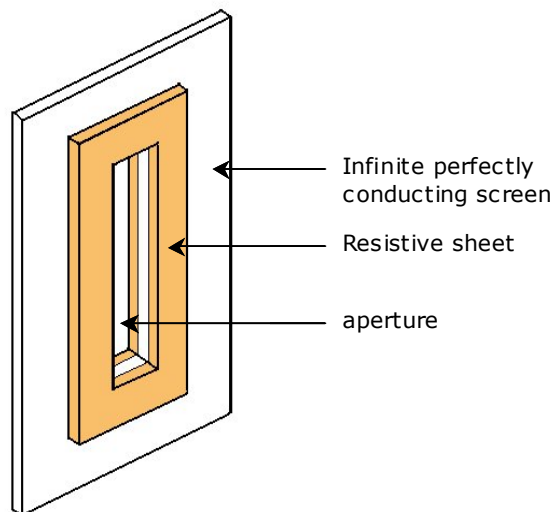
Figure 4.9 Configuration C. The resistive sheets are placed on top of the conductor from both sides.
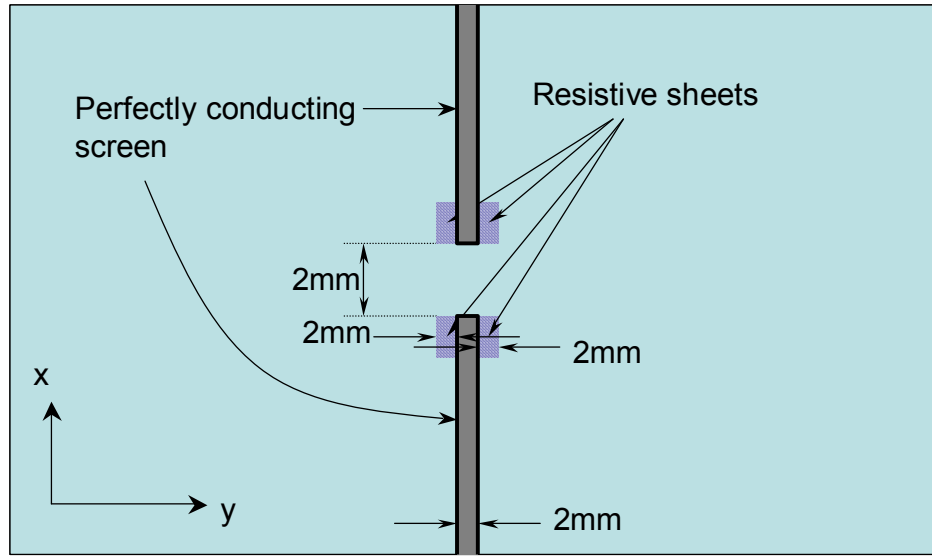
Figure 4.10 Cross section (x-y plane) showing the application of resistive sheets in Configuration C. Notice that the resistive sheets are applied on both sides of the screen.
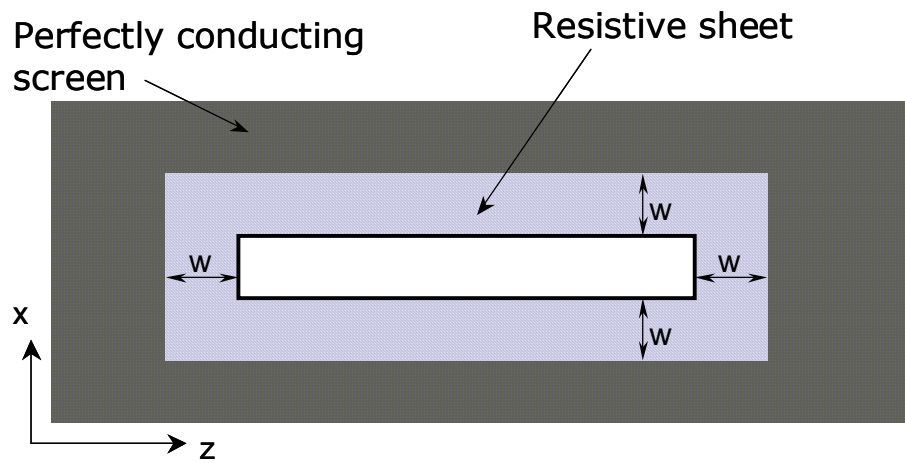
Figure 4.11. Front view of the aperture with resistive sheets of width w.

4.4   Numerical Simulation of Aperture Radiation

The aperture considered in this study is rectangular, measuring 2 mm x 20mm. The aperture is positioned in an infinite, 2 mm thick, perfectly conducting screen. The commercial FDTD-based code, EZ-FDTD^{TM} [24] is used for all the FDTD based simulations presented in this chapter.   The FDTD computational model for this aperture is shown in Fig. 4.12. The field source is an impressed current source with a differentiated Gaussian temporal profile sufficient to generate appreciable energy up to 20 GHz. The current source is polarized in the x-direction for maximum aperture radiation (see Fig. 4.12). The electric field is captured at the other side of the aperture and transformed to the frequency domain by Fourier transformation. The source and the monitor point are each 40 mm away from the plane of the aperture in opposite directions with respect to the aperture such that the source and monitor points lie along an axis that is normal to the aperture and that intersects the aperture at its center. The FDTD method cell size is $\Delta x=\Delta y=0.5$ mm and Δy ranges from 0.2 to 1 mm according to the resolution requirements of the simulation. A modified version of the Perfectly Matched Layer (PML) is used which is capable of simulating infinite conducting screens that are positioned normally to the computational domain. (Within this implementation of the PML, in effect, any perfectly conducting sheet that is positioned normally to the computational boundary is effectively stretched to infinity.) The computational domain is positioned 50-60mm away from the nearest edge of the aperture in order to minimize unwanted spurious reflections from the boundary of the computational domain. The text representing this model for EZ-FDTD input is attached to Appendix B.

Figure 4.12. FDTD computational domain used for the problem of field radiation through a 2mm x 20mm aperture placed in infinite perfectly conducting screen.
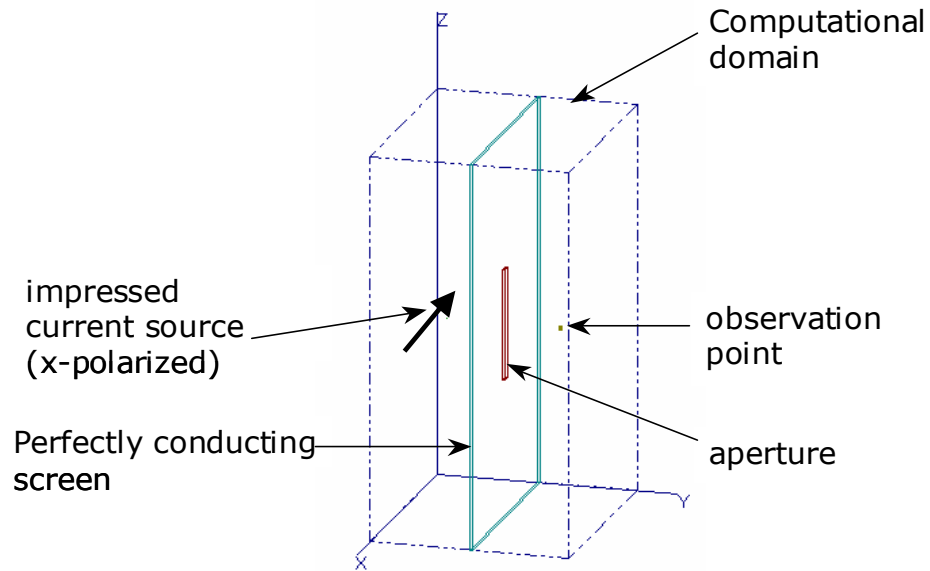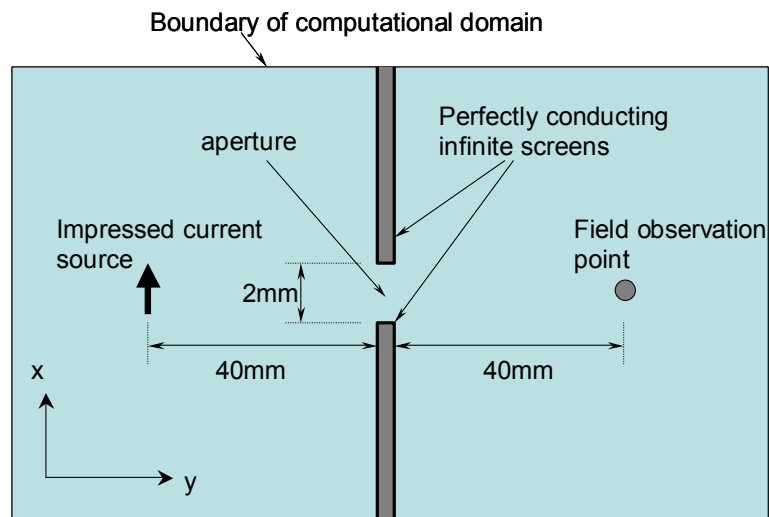

Figure 4.13 Cross section (x-y plane) of the FDTD computational domain showing source and field observation point placements.

4.5   Aperture Radiation Simulation Result

When the aperture is not loaded, maximum radiation, within the frequency range of 1-12GHz, occurs at approximately the frequency at which the aperture becomes resonant, which, for the aperture size considered here, is approximately 7.2GHz. The resistive sheet material considered initially are given by μ_r= 1, ε_r =4, and σ =5 Ohm^{-1}m^{-1}. In Fig. 4.14, we present the radiated field at the near–field monitor point (40mm away from the aperture as depicted in Fig. 4.13) for the x-polarized electric field. The same field at a distance of 160mm (which we can consider as a far-field point) is shown in Fig. 4.15. The width of the resistive sheet is w=2mm. From Figs. 4.14 and 4.15, we immediately conclude that Configuration C provides the highest field reduction in comparison to the configurations A and B. In fact, one can observe an appreciable field reduction at the resonant frequency when Configuration C is used, with an approximate reduction of 12dB from the case of the unloaded aperture.

Based on the transmission line model of the aperture, one would intuitively expect that Configuration A would yield the highest field reduction. It is important to keep in mind that the transmission line model (or interpretation) is only intended to provide a conceptual frame of reference to the field behavior within the aperture. Further insight can be gained by calculating the wave impedance within the aperture, which is defined as $|E_x/H_z|$. A simulation was conducted to test this definition of the aperture impedance, and the results, shown in Fig. 4.16, reveal that the impedance peaks at the center of the aperture and gradually decreases as the shorter edges of the aperture are approached. The monotonically decreasing wave impedance within the

aperture indicates that a tapered transmission line is a more accurate model of the aperture than a uniform line.

The fact that Configuration C is more advantageous than the other configurations from the shielding effectiveness perspective is a very welcomed finding. Note that it was stressed earlier that the objective of this work is to maintain a mechanically robust aperture design, which also satisfies heat transfer requirements. Notice that configurations A and B require the presence of resistive sheets within the aperture. This requirement presents a challenge; as such configurations would require mechanical support due to the fragility of resistive sheets. Configuration C is mechanically stable, as the resistive sheet would be applied (coated) directly on the surface of the enclosure. For the remaining part of this chapter, results will be presented only for Configuration C.
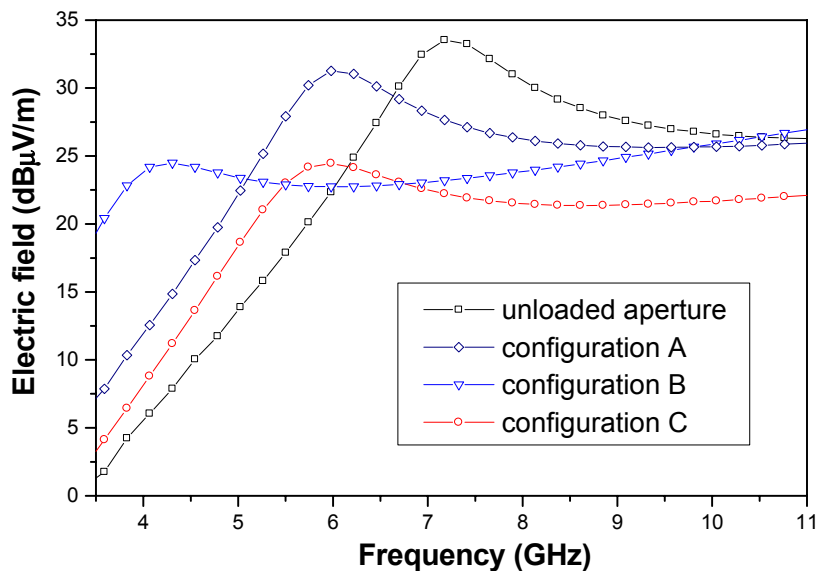

Figure 4.14 Radiated electric field (x-polarization) at a distance of 40mm from the aperture.
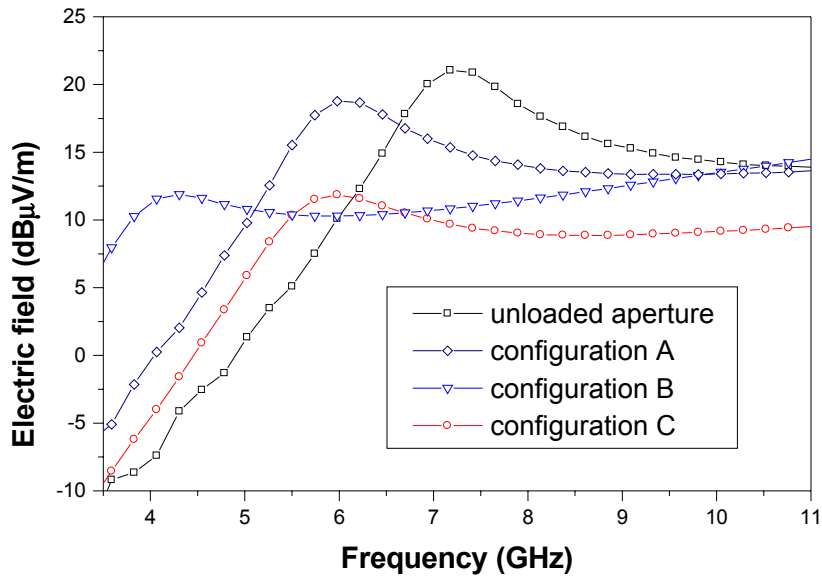
Figure 4.15 Radiated electric field (x-polarization) at a distance of 160mm from the aperture.
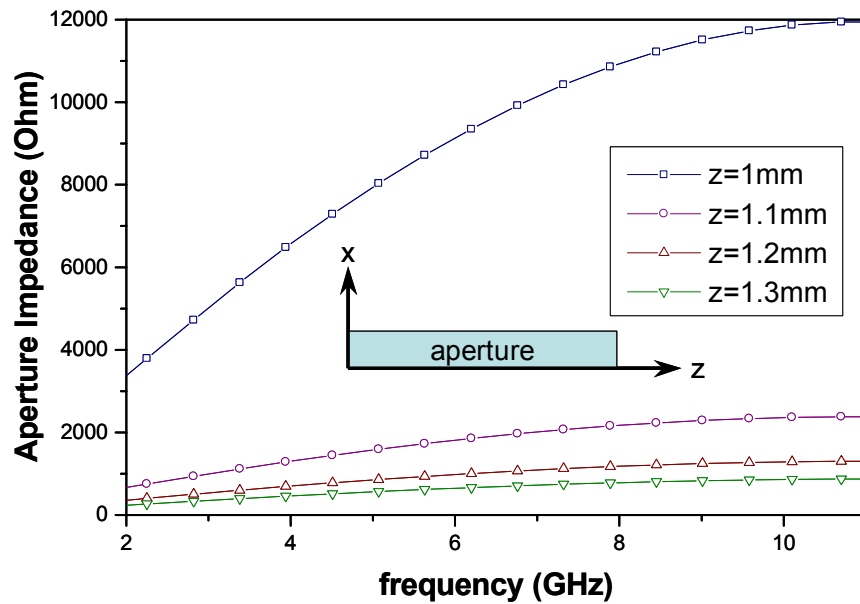
Figure 4.16 Aperture impedance, defined as |Ex/Hz|, at different locations within the aperture. z=0 and z=2mm correspond to the beginning and end of the aperture, respectively.

The results presented in Figs. 4.14 and 4.15 were for a resistive sheet of w= 2mm. The effect of increasing the width from w=1mm to 12mm, while keeping other parameters at μ_r= 1, ε_r =4, and σ =5 Ohm^{-1}m^{-1}, is shown in Fig. 4.17 for the same field polarization and near-field observation point as before. Notice that the case of w=6mm offers the highest field suppression. For w higher than 6mm, the radiated field starts to increase at and beyond the resonant frequency.

The effect of varying the conductivity, while keeping the permittivity, permeability and sheet width, w, constants, is shown in Fig. 4.18. The results shown in Fig. 4.18 for higher conductivity were obtained while insuring that the field penetration through the resistive sheet is resolved. Throughout the FDTD simulations, the cell size in the y-direction (normal to the resistive sheets) was maintained at or smaller than 1/10 of the shortest wavelength considered in the simulation. It is noted with interest that increasing the conductivity of the resistive coating has a diminishing effect on the radiating field at or close to the resonant frequency of the aperture, while having a pronounced effect at other frequencies.

The effect of varying the permittivivity while keeping the conductivity, permeability and sheet width constants, is shown in Fig. 4.19. It is observed that varying the permittivity within the range considered has minimal effect on the radiated field.
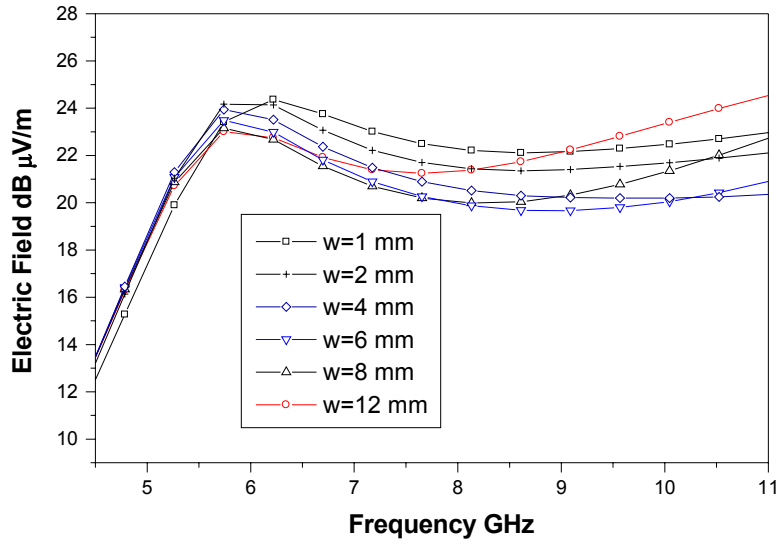
Figure 4.17 Effect of varying the width of the resistive sheets on radiation for Configuration C with $\mu_r= 1$, $\varepsilon_r =4$, and $\sigma =5$ Ohm^{-1}m^{-1}
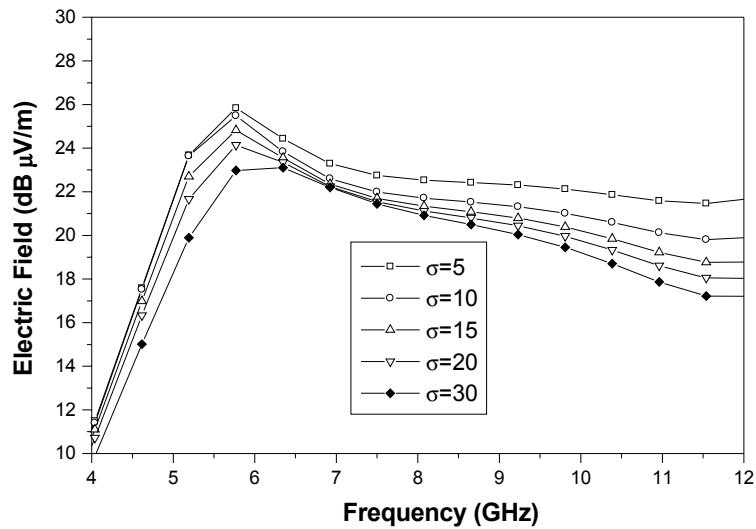
Figure 4.18 Effect of varying the conductivity on the radiated field for Configuration C with $\mu_r= 1$, $\varepsilon_r =4$, and w=6mm.
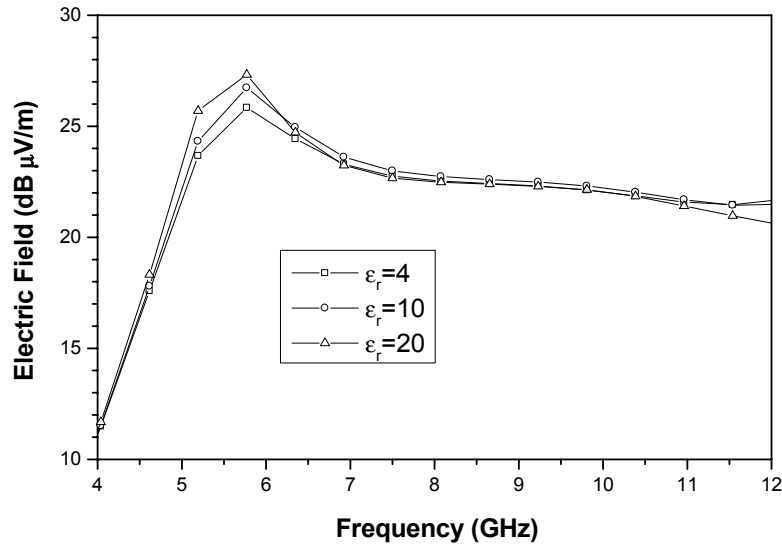
Figure 4.19 Effect of varying the permittivity on the radiated field for Configuration C with $\mu_r= 1$, $\sigma=5$ Ohm^{-1}m^{-1}, and w=6mm.

From the above empirical analysis, we conclude that a reduction of the radiated field of up to 13dB can be achieved if Configuration C is used with ε_r and σ both lying within the ranges considered, and with a sheet width, w, of 6mm. Amongst the material design parameters considered in this study, the width of the sheet was found to be the most sensitive factor in affecting the shielding effectiveness of the coated aperture. Based on the results presented in Fig. 4.17, the relationship between the loaded aperture radiation and sheet width is a complex one, and is clearly highly frequency dependent. It is important to keep in mind that the radiation through the aperture is due to the direct field penetration through the aperture, and is also due to the electric current that is induced on the external side of the screen, especially in the immediate vicinity of the aperture. In Figs. 4.20(a) and (b), we show a calculation of the electric current density for two cases of unloaded and loaded apertures. In Fig.

4.20(b), we show the current density for Configuration C where the resistive sheet properties are $\mu_r = 1$, $\varepsilon_r = 4$, $\sigma = 5$, and w=6mm. Notice that the dipole-like behavior of the unloaded aperture is clearly visible in Fig. 4.20(a). The effect of loading the aperture is shown to dramatically reduce the electric current density on the external side of the screen, thus leading to reduced external radiated field.
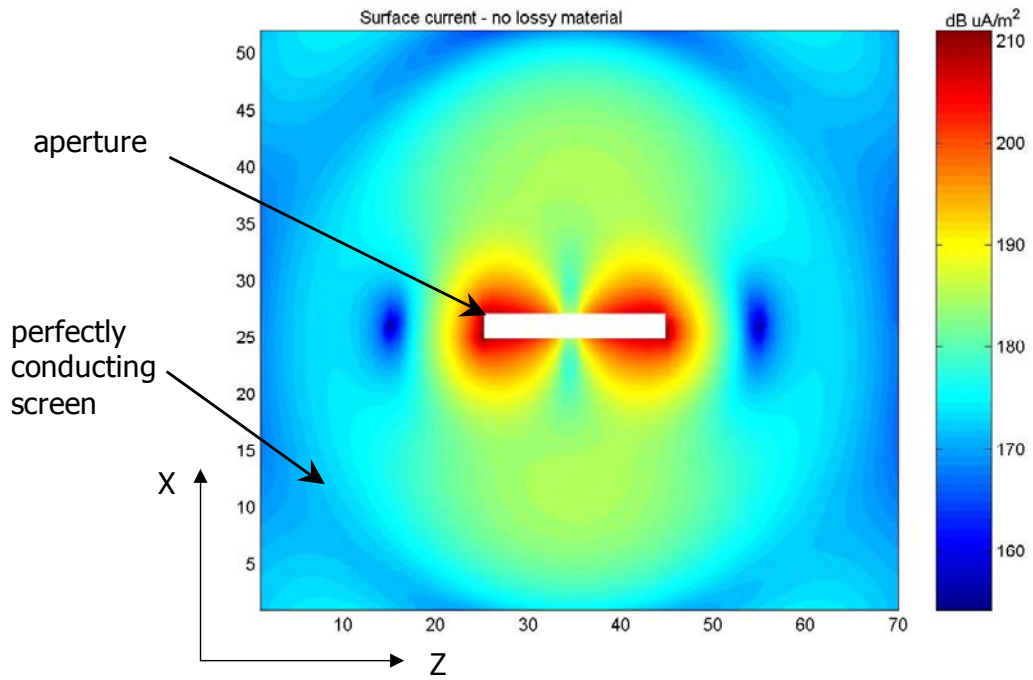
(a)
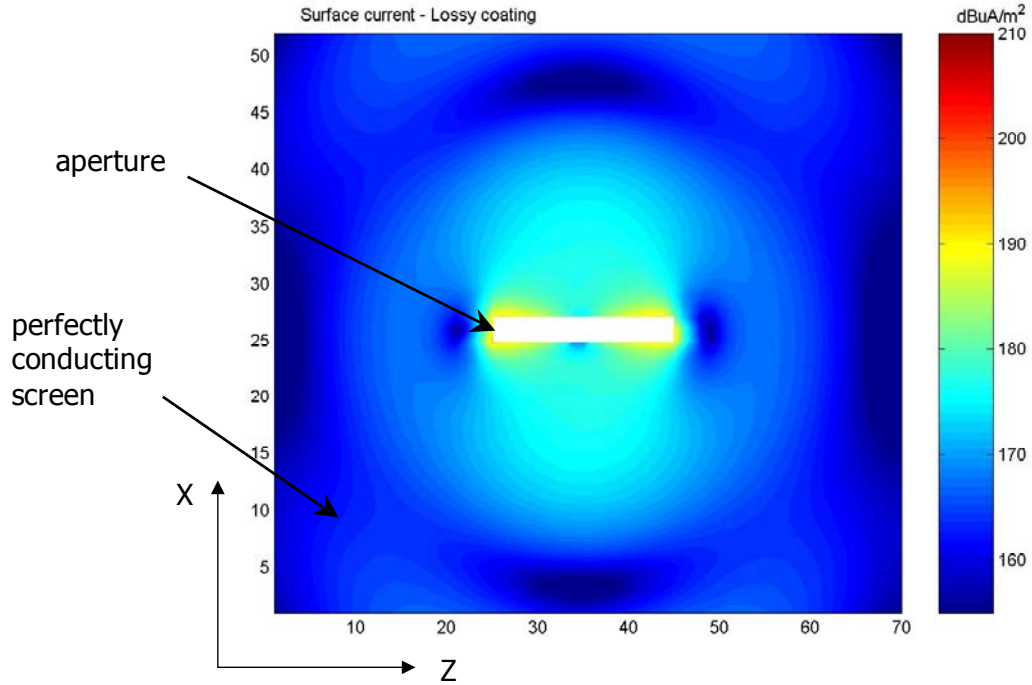
(b)

Figure 4.20 Total surface current density at the external surface of the screen at 7.2GHz. (a) Unloaded aperture, (b) Loaded aperture: Configuration C with $\mu_r= 1$, $\varepsilon_r= 4$, $\sigma=5$ Ohm^{-1}m^{-1}, and w=6mm.

4.6 Radiation from Loaded Circular Aperture

Electromagnetic scattering from multiple circular apertures and their mutual coupling in a conducting plane has been studied extensively [25]-[27]. However, the problems of penetration from single circular aperture and the method of radiation mitigation are not thoroughly considered. This section will present the numerical solution of the radiation through a circular aperture on an infinitely large conducting wall and the mitigation technique.

HFSS is selected to simulate circular structure because of the capability of treating complex geometry. HFSS is a commercial three-dimensional full-wave Maxwell equations simulator developed by Ansoft Corporation. A circular aperture with 12mm radius on a 2mm thick large conducting plane is modeled using HFSS. A dipole antenna, 20mm long, 40mm away from the aperture will be the source of electromagnetic energy that can go to the other side of the conducting plane only through the circular aperture. The primary electric field is Z-polarized will be calculated 40mm away from the aperture (the aperture is in the y-z plane as shown in Fig. 4.21. Dielectric lossy material will be applied to the circular aperture following the configuration illustrated in Fig. 4.9 but with circular shape (see Fig. 4.21).
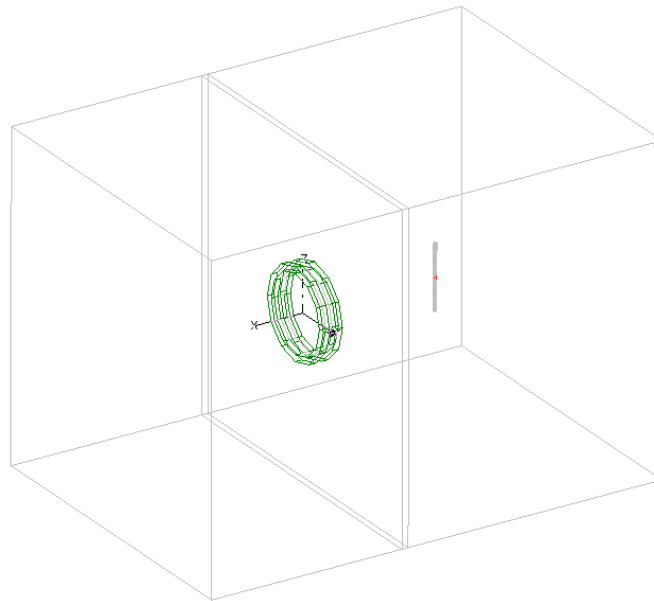
Figure 4.21 An HFSS model of a circular aperture in a large conducting plane.

By applying the 2mm wide, 2mm thick material (Fig. 4.21) with $\varepsilon_r= 4$, $\sigma=20$ siemens/m, the radiation through circular aperture is mitigated by about 3 dB in the

frequency range from 7.5-8 GHz (Fig. 4.22). This mitigation is not be as noticeable as the rectangular aperture. Further consideration of the material width, material permittivity, and material conductivity will be presented.
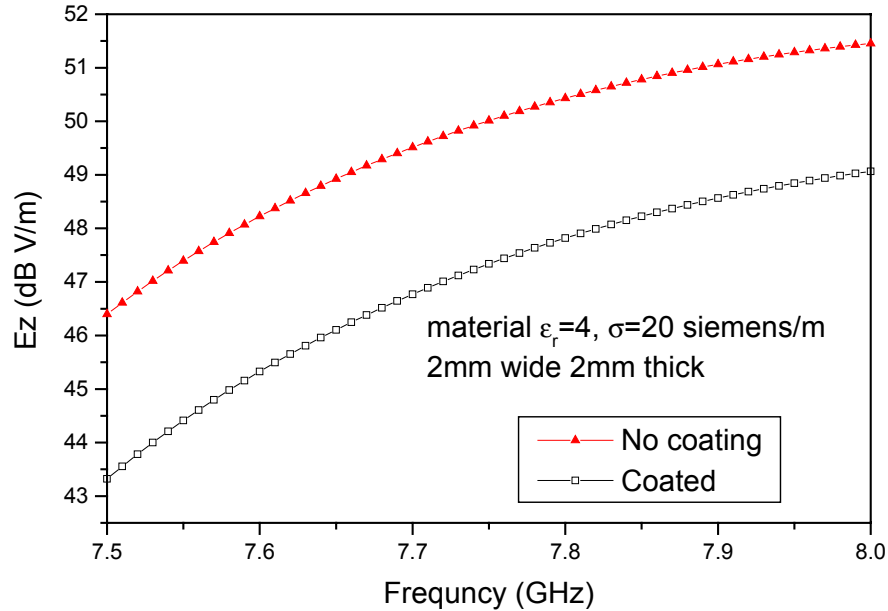
Figure 4.22 Radiation mitigation by applying lossy material to circular aperture

The results presented in Fig. 4.22 are for a resistive sheet of w=2mm. The effect of increasing the width from width of 2mm to 12mm, while keeping other parameters constant at μ_r= 1, ε_r =4, and σ =20 Ohm^{-1}m^{-1}, is shown in Fig. 4.23 for the same field polarization and near-field observation point as before. Notice that the case of 6mm width offers the highest field suppression. For width higher than 6mm, the radiated field starts to increase considerably in frequency range of my concern.

The effect of varying the conductivity, while keeping the permittivity, permeability and sheet width constants, is shown in Fig. 4.23. The results shown in

Fig. 4.23 for higher conductivity were obtained while insuring that the field penetration through the resistive sheet is resolved. It is noted that increasing the conductivity of the resistive coating reduces radiation in the low frequency but has fewer effect to the radiation as the frequency go higher.
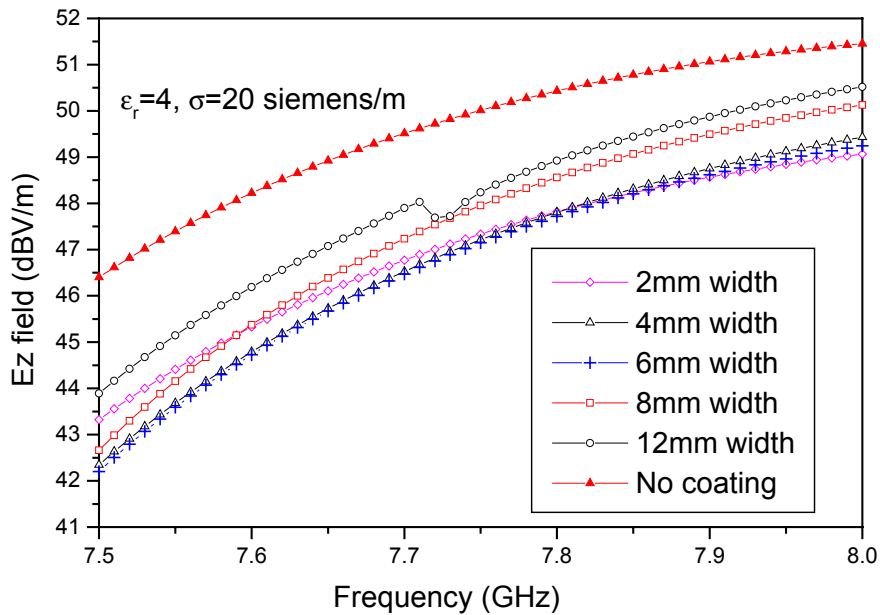
Figure 4.23 Effect of varying the width of the resistive sheets on radiation for material $\mu_r= 1$, $\varepsilon_r =4$, and $\sigma =20$ Siemens/m

The effect of varying the permittivity while keeping the conductivity, permeability and sheet width constant, is shown in Fig. 4.25. It is observed that increasing the permittivity has a significant effect on the radiation mitigation.
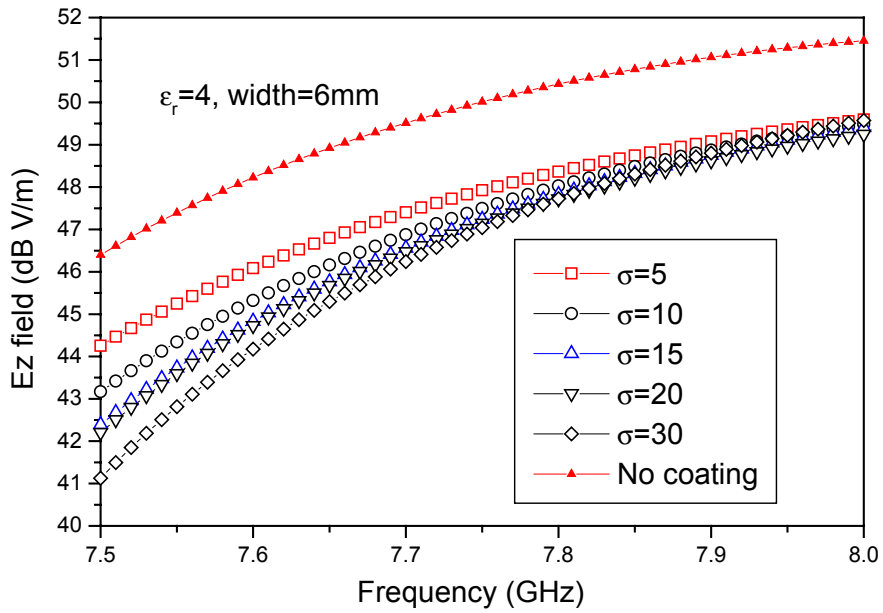
Figure 4.24 Effect of varying the conductivity on the radiated field for with $\mu_r = 1$, ε_r =4, and width=6mm.
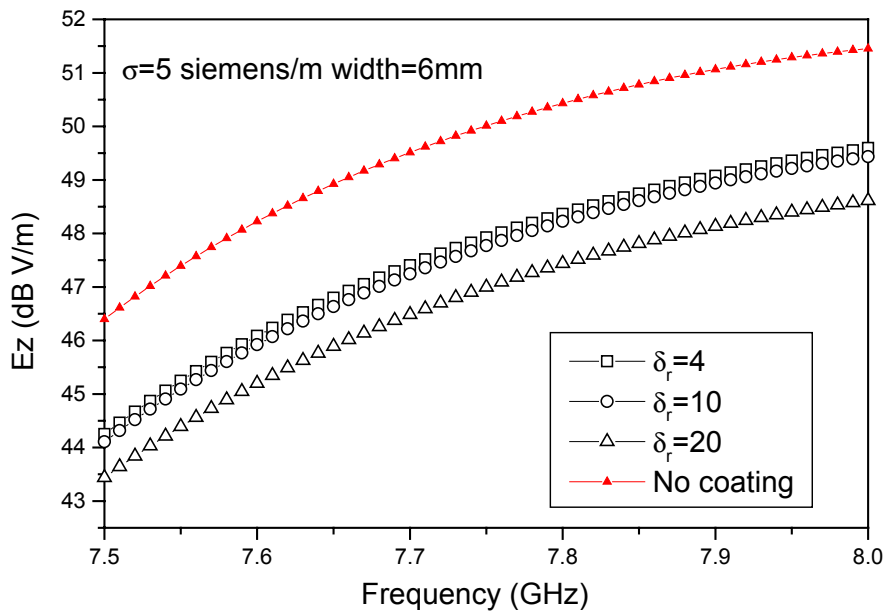
Figure 4.25 Effect of varying the permittivity on the radiated field for with $\mu_r = 1$, σ=5 siemens/m, and width=6mm.

4.7 Summary

The novel use of resistive sheets to reduce electromagnetic penetration through apertures while maintaining robust mechanical design is introduced. The use of resistive sheets or coating, was motivated by the interpretation of the aperture and the oscillating field within the aperture as a transmission line system. Based on this interpretation, a resistive material was applied in different configurations to minimize aperture resonance. Several resistive sheet configurations were tested numerically using the FDTD method. One of the configurations tested was found to yield optimal field results with up to 13dB reduction in the aperture radiation in comparison to the case of the unloaded aperture. Such appreciable reduction in the field was made possible using only a 6mm wide strip of a resistive sheet on both sides of the aperture. Finally, it is emphasized that this study is empirical. A more exhaustive optimization is the subject of a future study in which the material properties and topology of the resistive sheets are considered.

As a final note, we make a comparison between the loaded aperture discussed in this work and the work performed previously on loaded monopole and dipole antennas. In earlier works, resistive loading, consisting of coating an antenna with lossy material, was used with great effectiveness in increasing the broadband potential of the antenna and thus its potential for effective matching to a purely resistive transmission line system (there are numerous publications on the use of resistive coating of antennas; the interested reader is advised to study the original paper on this subject by Wu and King [28]). Based on Babinet's principle, the

aperture is the dual of the monopole and one would expect that a resistively loaded aperture, in the context of the definition used in this work, would have an analogous effect to that of the resistively loaded dipole. In fact, loading the dipole typically achieves a broadband behavior, however, at the cost of decreased efficiency. It is interesting that one notices a highly similar scenario in the case of the loaded aperture. Careful observation of Fig. 4.14, for instance, shows an increase in the broadband potential for the loaded aperture, i.e., an increased radiation at frequencies below resonance while an appreciable decrease in radiation at resonance. It is obvious that our objective in this work was to reduce radiation at resonance, but one can also think of this objective as widening the impedance bandwidth of the aperture.

Chapter 5 Radiation through Cavity-Backed Loaded Apertures: Experimental Study

The simple model of aperture in an infinite large plane is studied in the previous chapter. This ideal structure, however, hardly has any direct relevance in the real world. The apertures and seams we typically observe are usually part of the configuration of the enclosure. Some apertures are formed intentionally for air ventilation and heat dissipation. Other apertures could be unintentionally formed as the joint of two sides of enclosure. Radiation induced EMI is determined by the leakage through these openings for air ventilation and heat transfer purpose on the enclosure. The concern of this chapter will be the radiation through the aperture backed by metal enclosure and the technique to mitigate the electromagnetic interference.

Energy coupling between cavity mode and aperture has been studied analytically and numerically [29]-[34], while experimental investigations are limited. Dielectric material is used for reducing radiation or tuning bandwidth purpose. Polycaropu demonstrated how placing ferrite/dielectric in the cavity and covering the aperture will affect the cavity backed slot antenna characteristics [35].

5.1 Cavity-backed Apertures

The radiation through the aperture transmitted to the space outside of the cavity distributes power by some patterns. We will capture the radiation pattern and

then decided the angle where the most radiation occurs. To reduce this maximum field will be the objective of this chapter.

5.1.1 Aperture Radiation Pattern

It is convenient to use HFSS to study the radiation pattern and find out the direction that maximum radiation occurs. The radiation pattern represents graphically the spatial distribution of radiation from an antenna as a function of angle.

To implement the cavity backed aperture radiation study, a stainless steel enclosure is build. The rectangular enclosure measuring 250×200×150 mm is excited by a probe touching both top and bottom of the cavity. The power is input to the cavity through coaxial cable that joins the cavity by an SMA connector. The core of coaxial cable is connected to a probe vertically across the cavity and ended to the bottom surface with a 50ohm resistor. The radiation pattern is calculated by HFSS at frequency 3.7GHz around which the aperture resonates. The electromagnetic energy will leak through the 40×2 mm aperture in front side of the cavity.
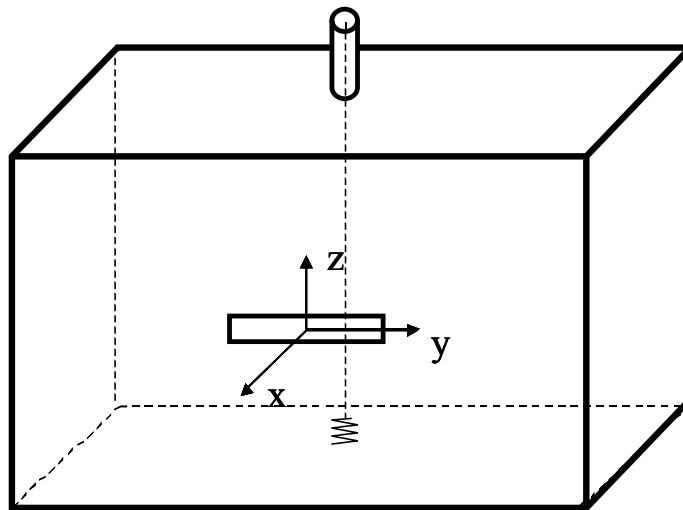
Figure 5.1 The 40mm aperture backed by cavity model with coordination

Fig. 5.2 shows the radiation patter as a sphere shape in a 3D view with the coordination system illustrated in Fig. 5.1. The shape of the primary Z polarization electric field radiation pattern is basically a sphere that maximum radiation occurs in x axis direction. By cross sectioning the sphere at azimuthal angle φ=0 which is a vertical cut normal to the aperture. Figure 5.3 shows us the Z polarization electric field with respect to the polar angle θ at frequency 3.7GHz. These two radiation pattern graphs suggest that the maximum radiation occurs along the x-axis. I will focus on E_z field since it is the dominant electric field.
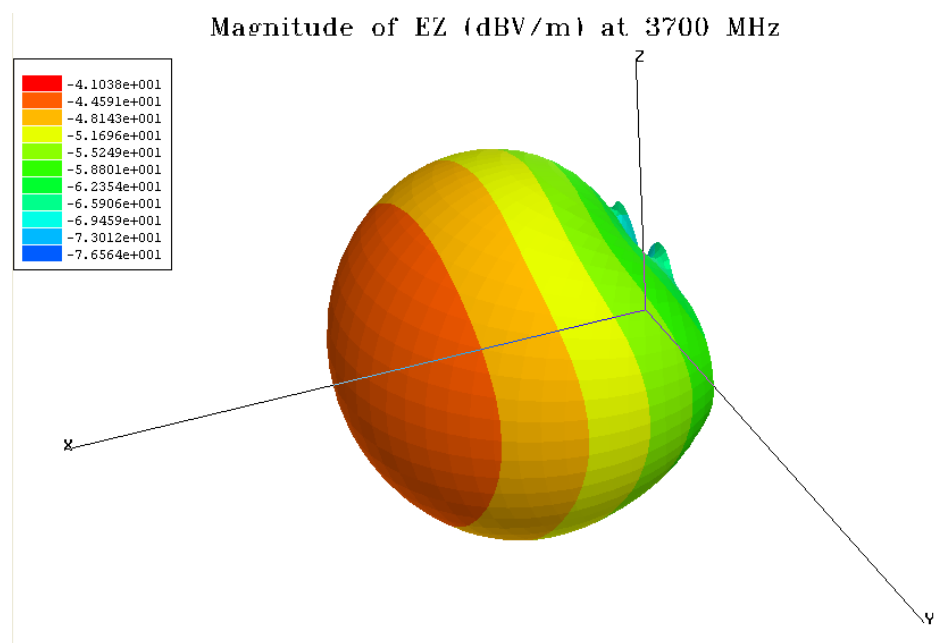
Figure 5.2 Radiation pattern of Z polarization field from aperture without loading by HFSS
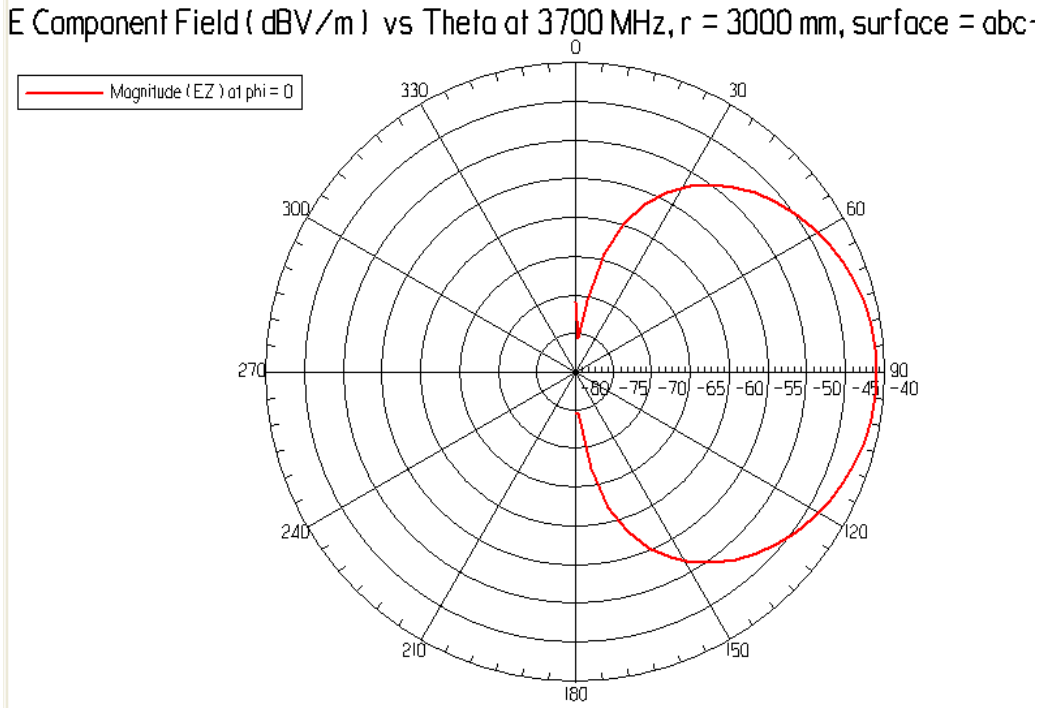
Figure 5.3 Electric field magnitude pattern with respect of θ

5.1.2 Power Transmitted into Cavity

The energy radiated through the aperture is affected by the power delivered into the cavity. Only at certain resonant frequencies, the power will be accepted by the cavity. The power accepted by the cavity will give us basic idea of the profile of power supplied to cause radiation.

The S_{11} parameter of the input will tell us how much power goes into the cavity in the frequency range. The ratio of delivered power to the enclosure to the incident power, presented by η, is calculated from S_{11} measurement by equation 5.1. The power delivered ratio is depicted in Fig. 5.4. It shows that the power delivery is maximized at those resonant frequencies.

$$\eta = 1 - \left| S_{11} \right|^2 \qquad (5.1)$$
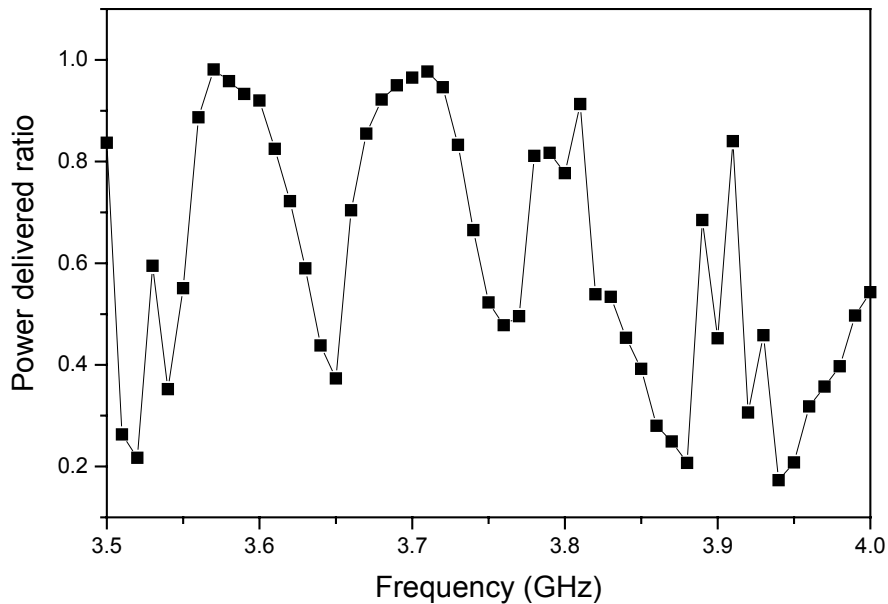
Figure 5.4 Delivered power to the cavity

5.2   Apertures Loaded with Dielectric Lossy Material

The resistive material or lossy material loading can reduce the radiation through aperture in infinite large plane according to the numerical result from chapter IV. We will implement the numerical and experimental work to see how the lossy material loading will effect the radiation through aperture backed by cavity.

The loading has the same configuration as we described in Fig. 4.9. The material has a thickness of 0.76mm and width of 6mm. The lossy material is from the Emerson and Cumming with model number VF-30. The specification by the manufacture states that it has dielectric constant of 37 at 8.6 GHz, with conductivity range of 2-20 siemens/m.

5.2.1 *Field Strength Numerical Simulation Result*

The cavity with aperture model is constructed by EZ-FDTD software shown in Fig.5.5. In the simulation the aperture is loaded with the VF-30 material, with the dielectric constant of 35 and conductivity of 20 siemens/m. The FDTD simulation runs 24 thousand time steps to get sufficient frequency resolution.
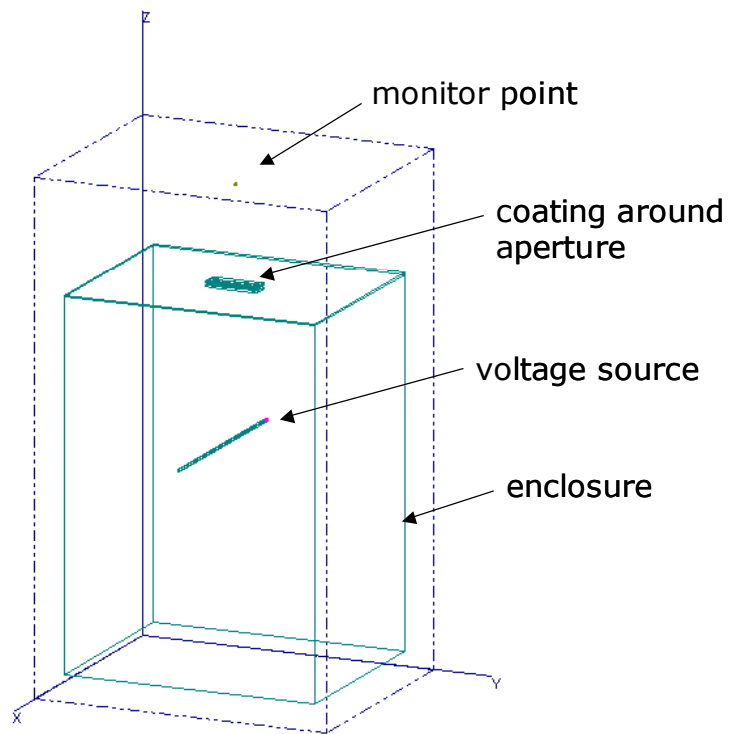
Figure 5.5 FDTD model of enclosure with loaded aperture

The electric field of x polarization in Fig.5.5 which is the major electric field is captured in front of the center of aperture and 40mm way from it. The following chart shows the effect of aperture loading to near field 4cm away from aperture. The peaks of the radiation agree with the peaks in the delivered power graph Fig.5.4. The lossy material loading around the aperture shows the effect of radiation mitigation in the overall frequency range shown in the graph although at aperture resonant

74

frequency 3.7GHz the field strength drops very little. The overall profile will be compared with experiment result in chapter 5.2.2.3.
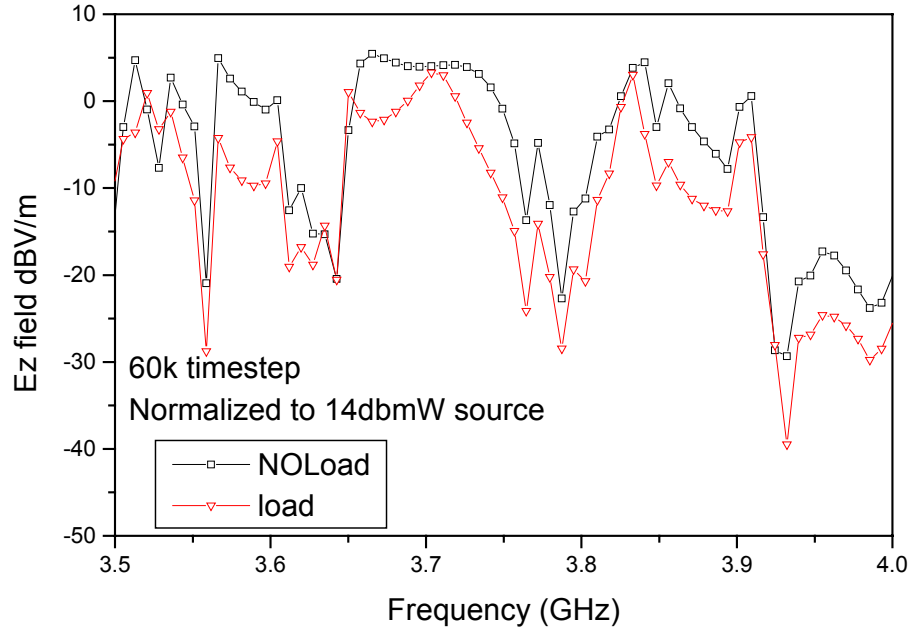
Figure 5.6 FDTD simulation of Ez field 4cm away from aperture

5.2.2 Experiment and Result

The testing of the radiation needs a probe to capture the field strength where the field is monitored in numerical model. A monopole antenna will be applied to implement the measuring task. To find the field strength, the induced voltage by the monopole antenna is measured in an anechoic chamber. The antenna factor of the monopole will be calculated to finally capture the field strength value.

The S_{21} parameter is an alternative to the field strength measurement since it may give us the same observation more efficiently. The S_{21} parameter will be measured when the probe is considered as receiving port. The result of the above testing will be compared to see the effect of lossy material loading.

5.2.2.1 S-parameters measurement

A 20mm long monopole probe is located 40mm away from the aperture to capture electric field there. The experiment setup is illustrated in Figure 5.6. The probe and the energy input port are both connected to the vector network analyzer by 50ohm coaxial cables.
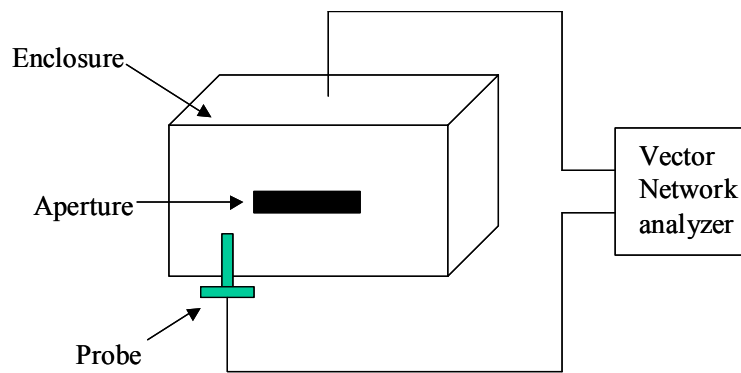
Figure 5.7 S_{21} experimental measurement setup

S_{21} measurement stands for the ratio of the voltage received by probe to the incident voltage to the enclosure. The square of S_{21} is therefore the ratio of power that delivered to the probe to the power that provided by the source. The field strength at the probe is decided by the power it receives. Ignore the reflection that the small monopole brought to the field, the power received by the monopole probe will characterize the field strength at the location that radiated through the aperture.

The experiment is repeated after applying the material as configuration in Fig. 4.9 with thickness of 0.76mm and width of 6mm. The S_{21} is reduced considerably in 3.5-4GHz by the lossy material loading as shown in Fig. 5.8.
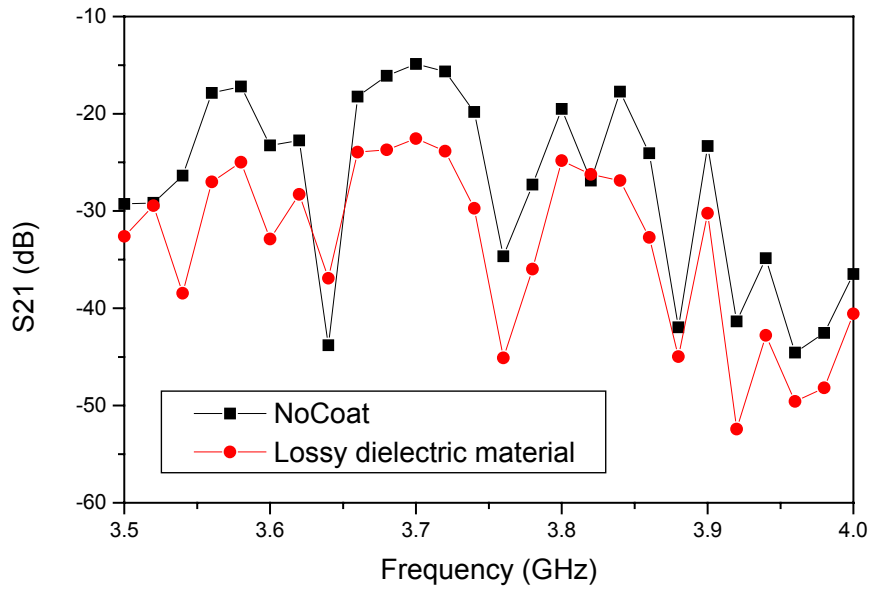
Figure 5.8 Effect of VF30 material loading to S_{21} parameter

5.2.2.2 Induced voltage measurement

The near field measurement is implemented in the anechoic chamber by the monopole 4cm away from aperture. The testing system includes the continuous wave generator and spectrum analyzer as shown in Fig. 5.9. The continuous wave generator is tuned to output 14 dBmW power by 50 ohm coaxial cable to the enclosure. The spectrum analyzer measures the monopole antenna induced voltage, which is directly related to field strength through antenna factor (equation 5.2). The effect of near field mitigation by the same absorbing material as in chapter 5.2.2.1 will be measured in the testing.
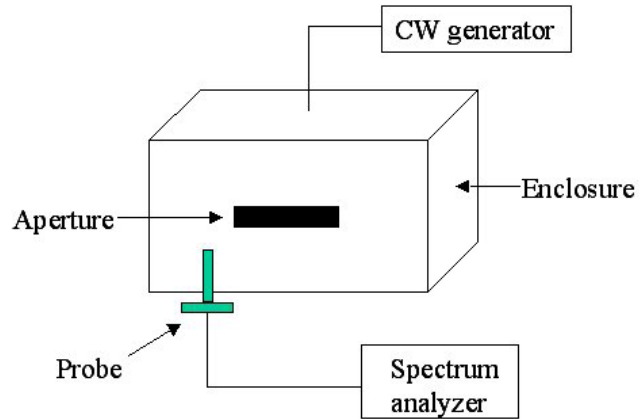
Figure 5.9 Probe induced voltage measurement setup
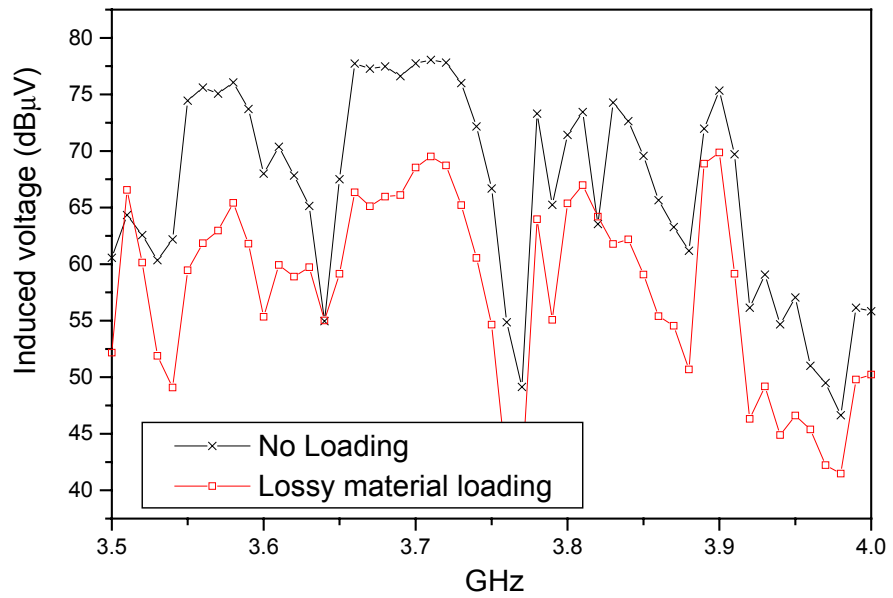
Figure 5.10 Effect of VF30 material loading to the induced voltage

The profile of S_{21} parameter in Fig. 5.8 and the induced voltage in Fig. 5.10 match each other very well. The radiation drops about 10 dB at the aperture resonance frequency around 3.7GHz.

5.2.2.3 Electric field calculation

To calculate the electric field, the antenna factor must be known. The antenna factor is the ratio of the electric field to the induced voltage:

$$AF = E / V \quad (1/m) \tag{5.2}$$

In general antenna measurements the gain and the directivity factor are predominantly specified. The equation (5.3) describing the relationship between the antenna factor and the practical gain is helpful, where λ is the wavelength.

$$AF = \frac{9.73}{\lambda\sqrt{G}} \tag{5.3}$$

The directivity of an ideal quarter wavelength monopole over conductive plane is 3.3 by theory. The gain of the antenna is calculated given the mismatch factor η:

$$G = \eta D \tag{5.4}$$
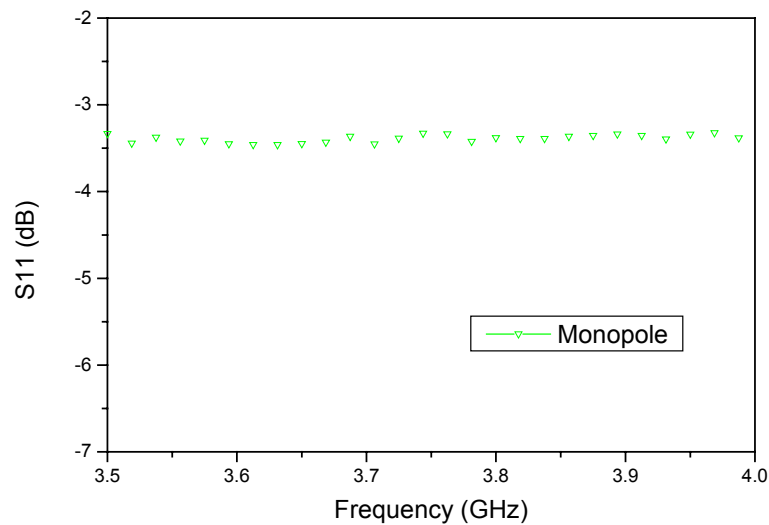
Figure 5.11 Monopole probe S_{11} feature

79

Since the factor η is related to S_{11} by equation 5.1, S_{11} of the monopole probe is measured first. Fig. 5.11 shows the S_{11} parameter of the monopole probe. The S_{11} of has -3 to -4 dB magnitude implies reflecting and hence receiving capability as well.

To consider the mismatch between directivity and gain I assume a perfect antenna that has all the accepted power radiated. The mismatch factor is then taken into account only with S_{11} parameter by equation 5.1. The cable loss in the experiment is assumed reasonably to be 6dB, which will be added to the voltage calculation finally. With equations 5.2-5.4 and S_{11} data above, we have the electric field calculation in figure 5.12.
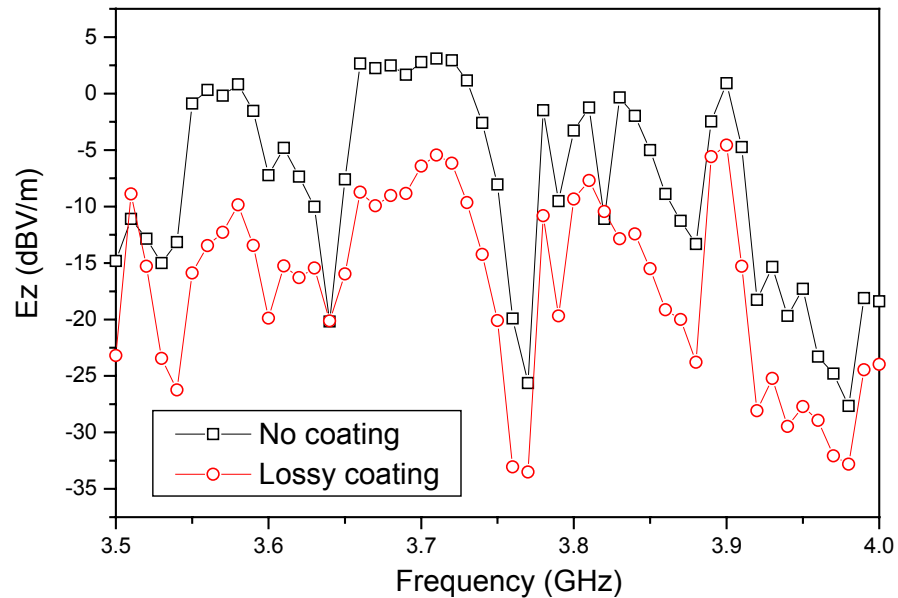
Figure 5.12 Electric field calculated from induced voltage

The electric field strength basically shares the same profile with the induced voltage in Fig. 5.10. That is partly because the S_{11} dependent mismatch factor is

largely flat in the frequency range of 3.5-4.0 GHz. The S_{21} parameter is closely related to the field strength as we can compare Fig. 5.8 and Fig. 5.12. For the convenience of the testing, I select S_{21} as the gauge to evaluate the radiated field without compromising integrity of the result.

5.3   Radiation Mitigation by Magnetic Material Loading

The surface current is induced when the electromagnetic wave reach the conductor. This surface current can flow to the other side of the conductor and may cause the radiation too. The mitigation of surface current is another way of thinking to mitigate the radiation through aperture.

5.3.1 The Mitigation of Radiation from Aperture

Based on the boundary condition of perfect conductor, the tangential electric field goes to zero at the perfect conductor surface while the tangential magnetic field is at a maximum. The material with high magnetic loss may have better dissipation performance for the magnetic field. Under this assumption, magnetic material will be applied to coat the aperture to reduce the surface current.

The magnetic material MCS from Emerson & Cuming is selected to coat the aperture. The coating has the same configuration as we described in Fig. 4.9. The material has a thickness of 1mm and width of 6mm. The permittivity and permeability specification by the manufacture is shown in Fig. 5.13 and Fig.5.14. In our frequency range of concern, the permittivity is about 37. The permeability is about 2 with loss tangent of 1.25 based on the curve.

The S$_{21}$ is measured using the same monopole antenna as we test the dielectric coating. The monopole is placed 40mm away from the aperture. The experiment setup follows the same configuration as in Fig. 5.7.
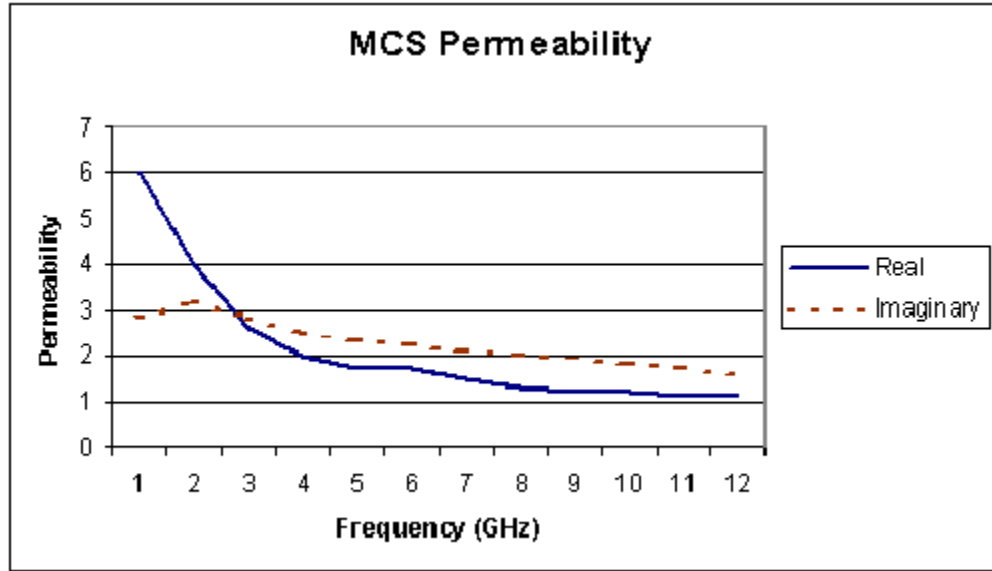
Figure 5.13 The permeability specification of MCS material
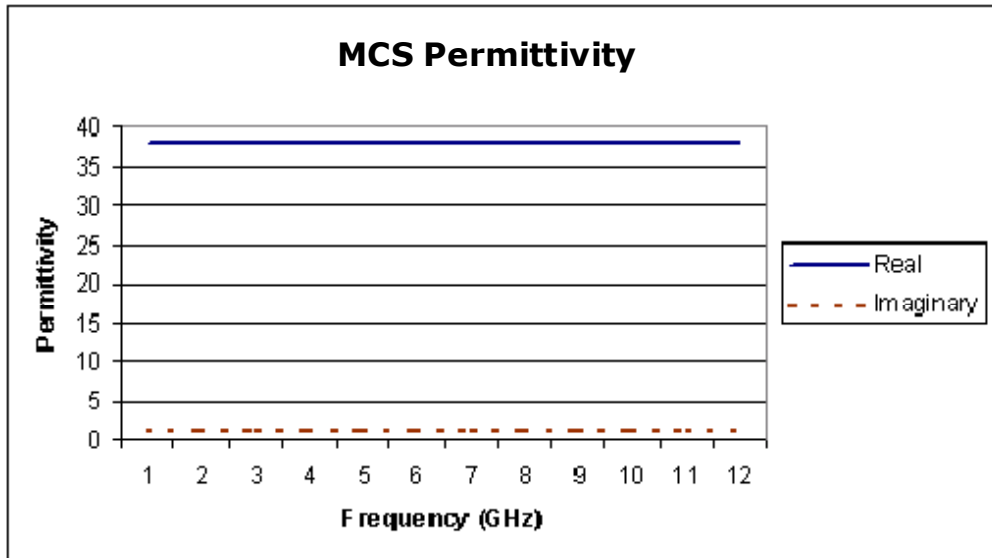
Figure 5.14 The permeability specification of MCS material

When the aperture is loaded with MCS magnetic material, the S_{21} parameter is reduced considerably. At 3.7 GHz, the S_{21} drops more than 10 dB as shown in Fig. 5.15.
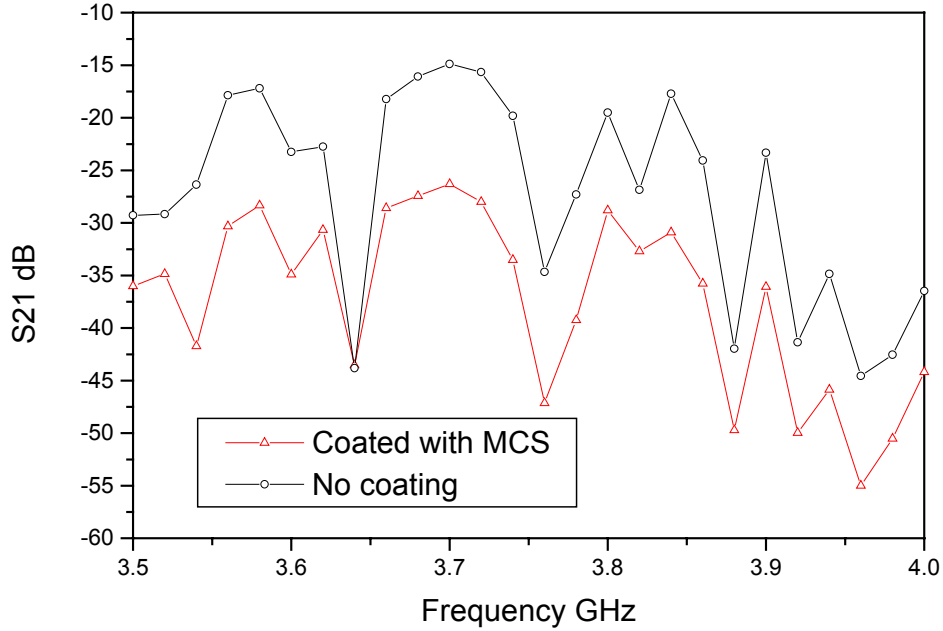
Figure 5.15 The S_{21} parameter measurement with MCS material loading

5.3.2 Comparison of Dielectric Material with Magnetic Material

The VF-30 and MCS are from the same manufacture with similar function of absorbing microwave energy. Their performance to mitigate the radiation through aperture is evaluated by the S_{21} change in Fig. 5.16.

The MCS magnetic material has better performance than the VF-30 dielectric material in our frequency range. However, the VF-30 is 0.76mm thick while the MCS is 1mm thick. There is not enough evidence to assert the advantage of magnetic material over dielectric material. It is hard to explicitly characterize the effect of

single material property (permittivity or permeability), since two kinds of material that have more than one property differs from each other. Numerical simulation may be the only feasible method to study material with any material property combination.
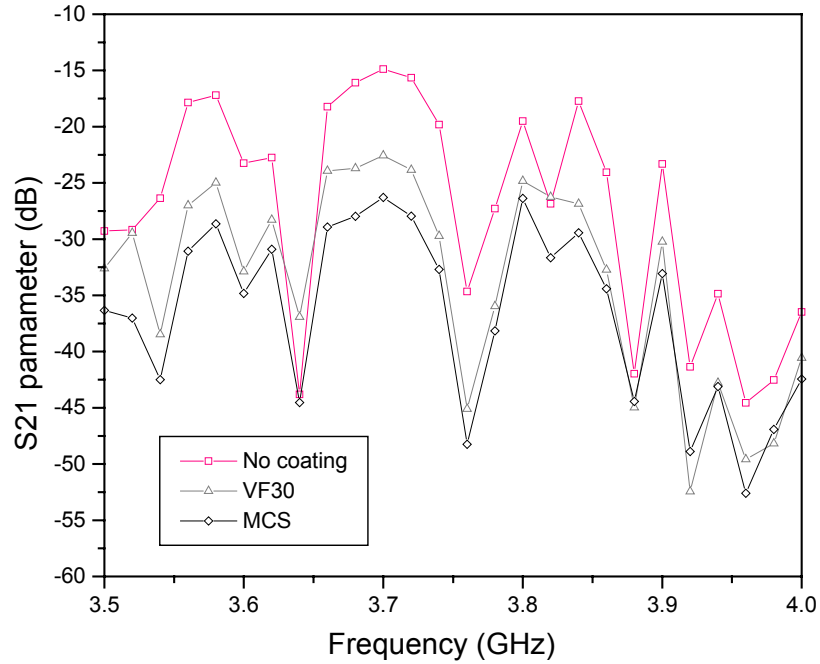
Figure 5.16 The comparison between VF-30 and MCS to mitigate radiation through aperture

VF30 is specified by manufacture that the insertion loss is 12dB in X band witch is from 2-4GHz. Compared with data provided by manufacture, the approximate 10dB mitigation is over the expectation since the material is only coated surrounding the aperture which does not block the area of aperture at all. The electromagnetic material properties of two materials provided by manufacture are listed in the following table.

	$\varepsilon^{'}$	$\varepsilon^{''}$	$\mu^{'}$	$\mu^{''}$
VF30 (at 8.6 GHz)	37	42.55	1	0
MCS (at 3.7GHz)	37	≈ 1	2	2.5

Table 5.1 Material properties of VF30 and MCS

5.3.3 Magnetic Material Dimension Effect

The magnetic coating we test in this chapter has very good performance in lower electromagnetic field penetration through aperture. Further improvement based on the coating that has the configuration in Fig. 4.9 will be the next question.

The width of the loading sheet is probably one of the factors that will change the performance. To see the effect of width of loading sheet, I prepared MCS material of different width including 6mm, 8mm, 12mm, and 18mm. The testing follow the S_{21} parameter testing implemented before. The result presented in Fig. 5.17 does not show big difference between the four different dimensions. However, the loading sheet with the largest width of 12mm does show better result than the others.
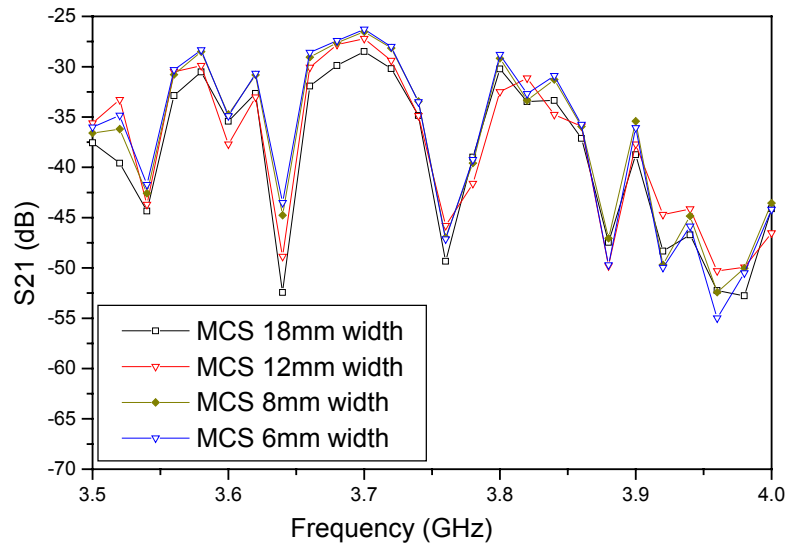
Figure 5.17 The effect of varying width of MCS magnetic material on the field penetration through aperture

The thickness of the material is another factor that needs to be considered. Based on the hypothesis that the H field will decrease quickly with the thickness of the magnetic material, the thickness of the material may not be very important. Given that the configuration in Fig. 4.9 is a double sides structure, the next question is which side in this configuration is more important and how it works compared with double sides configuration.

The situation that only one layer is loaded inside of the enclosure is named inside coating. Similarly the situation that only one layer loaded to the outside of the enclosure is named outside coating. The result shown in Fig. 5.18 suggests that the contribution of radiation mitigation is different between the inside and outside loading material. The effect of two sided loading suggests that the total mitigation might be the sum of each of the loading sheets.
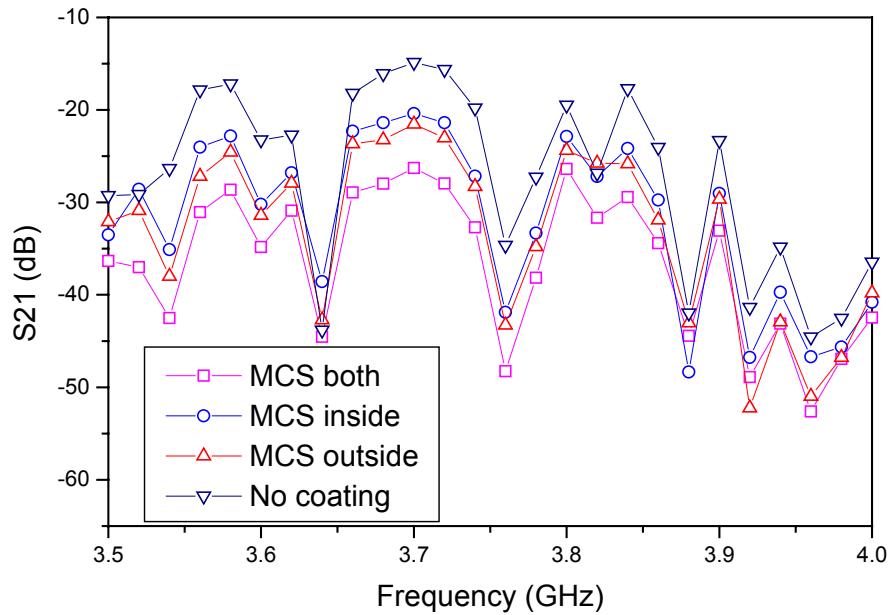
Figure 5.18 The effect of varying width of MCS magnetic material on the field penetration through aperture

5.4 Field Coupling into Enclosure

The radiation that comes out of enclosure has demonstrated to be considerably reduced by 10dB or more in the resonance frequency. This phenomenon comes up the question that how the loaded aperture works if the radiation travels the reverse direction. This kind of susceptibility experiment is very crucial in EMC testing and qualification.

The setup of this experiment is illustrated in Fig. 5.19. The transmitting antenna will radiate towards the enclosure with aperture. The aperture facing the transmitting antenna is the only path for electromagnetic energy to enter the enclosure. The transmitting horn antenna, which is working around 3.5 GHz, is

located 3m away from the aperture. This distance will reduce effect the reflection from the enclosure to the transmitting antenna since the enclosure has a much larger dimension than the transmitting antenna. A spectrum analyzer will measure the induced voltage with respect of the VF30 and MCS loading material. The loading material with 6mm width is coated to both sides of the aperture, following the configuration in Fig. 4.9. The power level of the continuous wave generator is set to 14 dBmW.
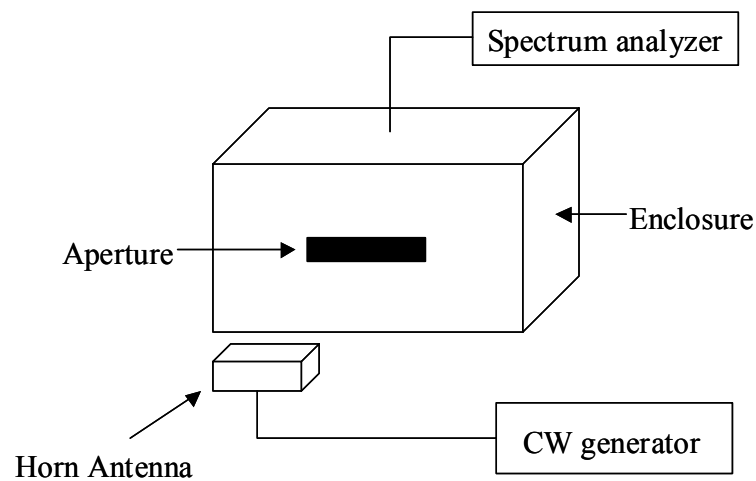
Figure 5.19 Susceptibility test setup with different loading material

The testing result in Fig. 5.20 shows that coupled energy goes into the enclosure is considerably lowered by the loading material around aperture. The magnetic material coating works better than the dielectric material. There is almost 10 dB drops for the magnetic material to lower the energy coupling. This technology will be very effective to improve the electromagnetic compatibility of the electronic device chassis in both the energy inward and outward consideration.
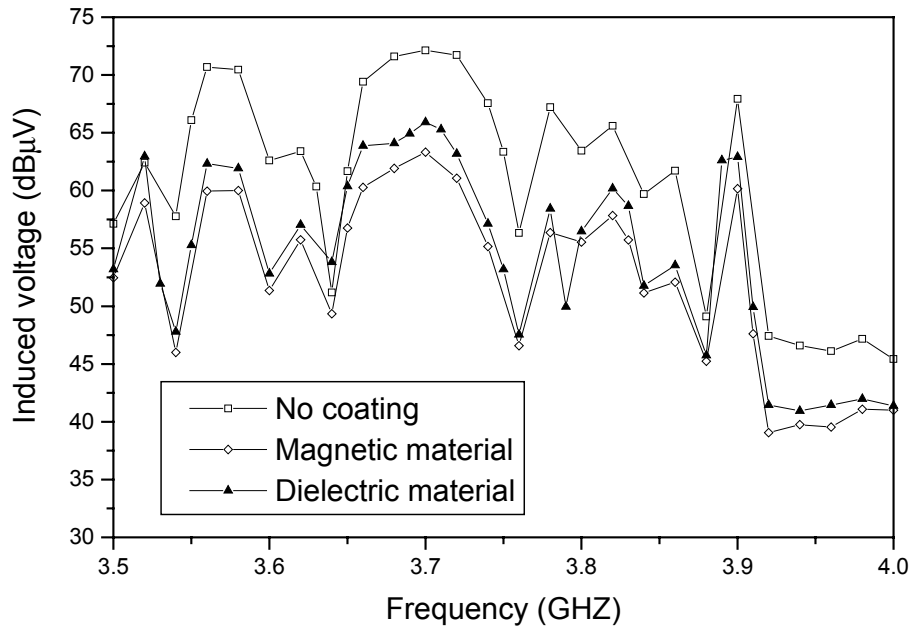
Figure 5.20 The induced voltage in susceptibility test with different loading material

Chapter 6 Thin Material Sheet Modeling

Dielectric has long been working as insulator mostly seen in capacitors. Its capability of holding energy can also be used in high frequency as well as in electrostatic mode. Thin dielectric layer is applied to high frequency components such as Microwave Monolithic Integrated Circuit (MMIC) amplifiers, radar random, printed circuit boards, and antennas. Thin dielectric substrates are used quite frequently in MMIC circuits such as MIM capacitors and spiral inductors. The modeling of thin dielectric material layer, either lossy or lossless, is crucial problem in numerical method.

6.1 Numerical implication of thin material

The use of thin material mainly benefit from saving the expensive microwave absorbing material. It is not always true that the thicker material will absorb more electromagnetic energy. Fig 6.1 shows the amplitude of reflected wave from a lossy material (ε_r=50, μ_r=1, σ=0.1 $\Omega^{-1}m^{-1}$) loaded to PEC wall with respect to the material thickness. The frequency of incident plane wave is 3GHz. The periodicity in Fig 6.1 suggests us that the using thin material can reduce the reflection to the some level as thick material does.
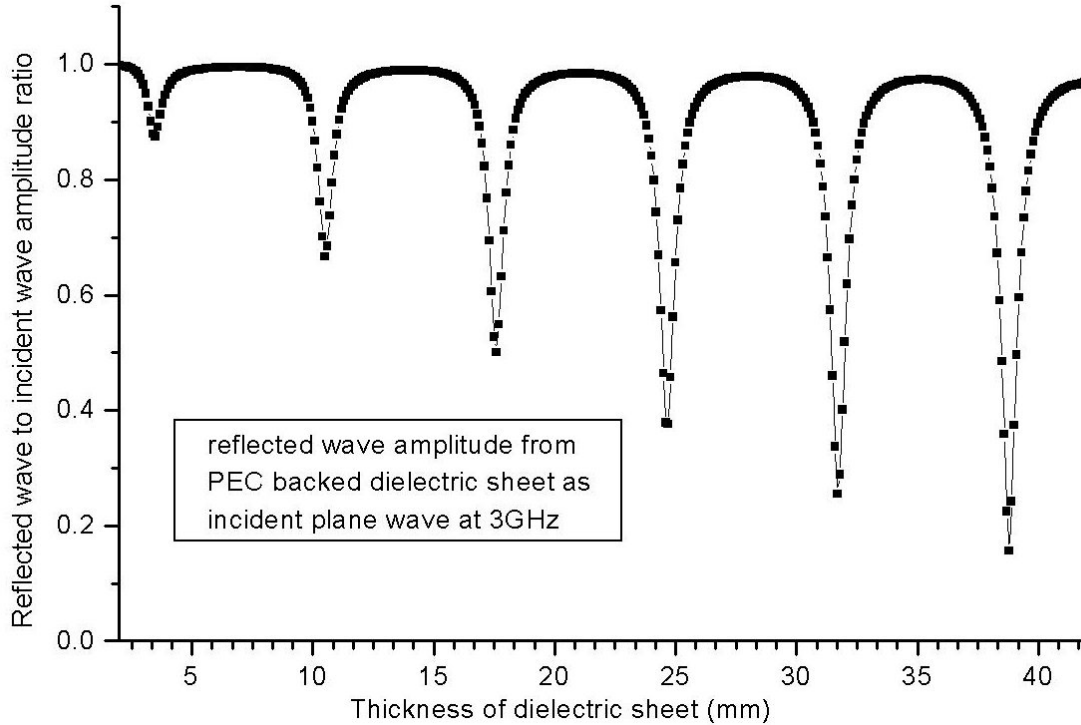
Figure 6.1 Effect of lossy material thickness to the amplitude of reflected wave from PEC backed lossy material sheet

How thin can we define as thin material? For lossless material, the judgment depends on the ratio of material layer thickness to the dimension of structure it is attached to. For lossy material, i.e. the conductivity of material is not very small, another criterion is based on the skin depth except for the geometry consideration. At higher frequencies, the resistance of conductor increases, because current tends to flow on the surface, only through an effective channel of depth, called the skin depth.

The skin depth will be derived from the propagation constant of a lossy medium defined in equation 6.1, where α and β are positive quantities, called attenuation constant and phase constant respectively.

$$\gamma = \alpha + j\beta = j\omega\sqrt{\mu\varepsilon_c} \tag{6.1}$$

$$\text{where } \quad \varepsilon_c = \varepsilon - j\frac{\sigma}{\omega} \tag{6.2}$$

σ-conductivity, ω-angular frequency

Skin depth is the distance from surface where the wave is dampened to $1/e$, defined as the reciprocal of α accordingly. Skin depth of a good conductor, which is under condition σ/ωε>>1, is defined in equation 6.3, where f is frequency.

$$\delta = \frac{1}{\alpha} \approx \frac{1}{\sqrt{\pi f \mu \sigma}} \tag{6.3}$$

FDTD has gained prominence amongst numerical techniques in electromagnetic analysis because of its straightforward field iteration formulation and the merit of time domain method. However, the need of FDTD to record the field value of every cell, which is uniform throughout the computation domain, requires large amount of computer memory. The cell size has to be equal or less than the smallest dimension since the first step of FDTD simulation is to discretize the computation domain to uniform cells and to specify the material properties to each cell. It is not cost efficient for FDTD to model fine structures because the cell size can be no larger than the smallest structure dimension. The finer the structure, the larger the number of cells in the computational domain.

The interest of applying thin film to inside of enclosure surface to tune the resonance performance, either to mitigate the resonance or change the frequency of resonance, is also a motivation of modeling thin sheet structure. In the case that he thickness of the thin sheet is very small compared to the enclosure dimension, we must have the cell size no larger than the thickness of thin sheet. So the number of

cells will be huge that requires too large memory and computation time that even the high-end workstation cannot afford the work. It is necessary to find method other than the normal FDTD code with regular mesh truncation to model thin material layer.

Since FDTD is based on the assumption that field strength is linear between sample points, the number of cells per wavelength is at least ten approximately. The shortened wavelengths in high-permittivity or high-permeability materials may greatly increase the memory and computer time required to perform a calculation. If the thin material is a lossy material, the FDTD modeling will be more complicated than that of lossless material. In high-loss material such as good conductor, the field will decay exponentially, as shown schematically in Fig. 6.2. It will be impractical to shrink the cell size so as to maintain the linearity between cells.

Figure 6.2 Field strength dampened in good conductor
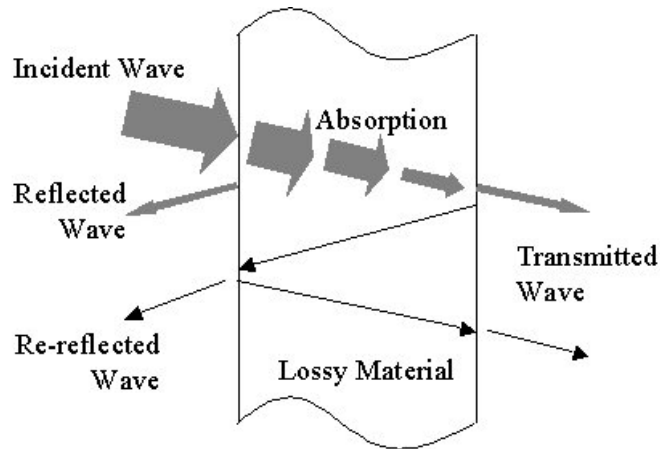
The enforcement of stability in FDTD requires that the progression from one node to the next, in any direction, does not exceed the speed of light. This physical constraint has a limiting effect on the relationship between the spatial step Δx, Δy, Δz and time step Δt, as in (6.4), where c is the speed of light in free space. However, the

speed of light in lossy material or good conductor is much less than that in free space, demand the Δt to be much smaller as well.

$$\Delta t \leq \frac{1}{c\sqrt{\dfrac{1}{(\Delta x)^2} + \dfrac{1}{(\Delta y)^2} + \dfrac{1}{(\Delta z)^2}}} \qquad (6.4)$$

In good conductor, under condition $\sigma/\omega\varepsilon \gg 1$, the speed of electromagnetic wave is

$$v = \frac{\omega}{\beta} \cong \sqrt{\frac{2\omega}{\mu\sigma}} \qquad (6.5)$$

Since the propagation velocity in lossy material is much smaller, the Δt limit becomes larger, hence relieve the time steps demand for modeling lossy material. However in models that have both lossy material and free space, Δt is decided by the by the smaller one, i.e. the time interval in free space. The computer memory is still the bottleneck for FDTD to model thin structure and lossy material.

One of the methods to treat lossy dielectric modeling is using surface impedance boundary. Surface impedance boundary is applied to treat the lossy material without changing mesh size in the FDTD code [36]. However, this frequency dependent technique has no advantages of time domain method and the capability to treat complex geometry. The transformation between frequency domain and time domain is sometimes quite complicated. Some techniques to model the thin material sheet in FDTD method are figured out using different principles [37]-[39].

6.2   Numerical Method for Modeling Thin Material Sheet in FDTD

Maloney came up with a method to model thin lossy sheet in free space [40]. This method has two key points: split the normal E-field to two parts with respect to free space and thin material in special grid where the thin sheet locates, and averaging the material property to update H-field. Fig. 6.3 shows the mesh truncation of FDTD and the normal E-field split. Following the same principle in, I incorporate the technique to a normal FDTD code modeling thin material sheet.
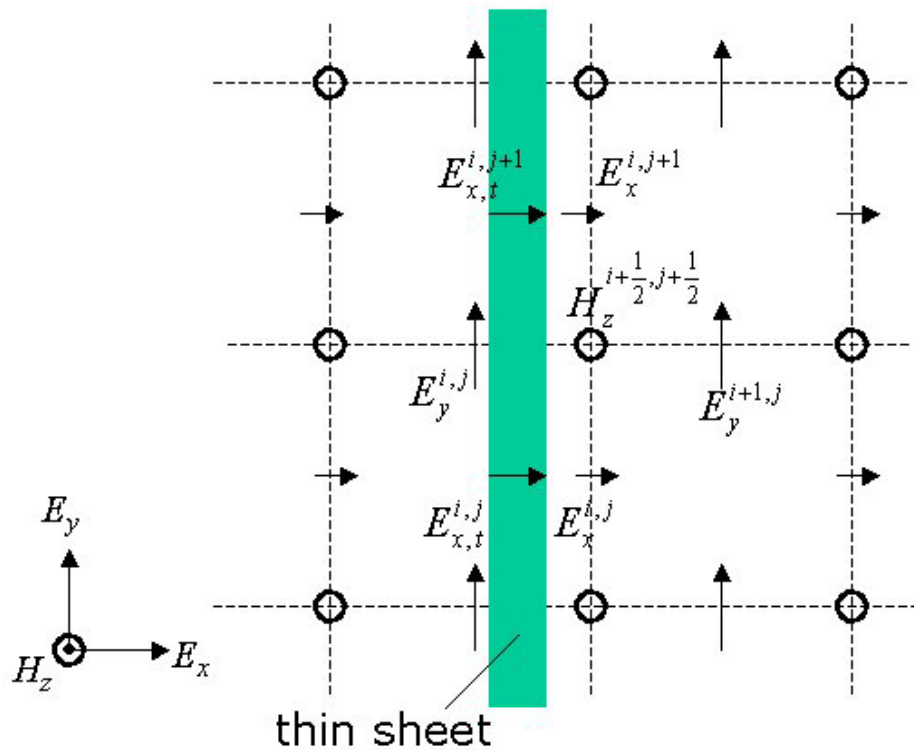
Figure 6.3 Mesh of FDTD where thin sheet locates

6.3 Result Validation

To verify the result of my code, I compare the numerical result with analytic solution. Lossless material sheet with ε_r=4, 10 and lossy material with ε_r=10, σ=10 $\Omega^{-1}m^{-1}$ are applied in free space to measure the reflected wave as shown in fig. 6.4. The frequency of the TEM incident wave coming from left is 5GHz with amplitude of 377V/m. Fig. 6.5 shows that the numerical result is equal to analytic solution for the lossless material sheet.

Fig. 6.6 shows the result comparison for the model with lossy material with material property ε_r=10, σ=10 $\Omega^{-1}m^{-1}$ where the incident wave is the same as the above model. Again, the code works very well with lossy material sheet.

Figure 6.4 Thin sheet in middle of free space
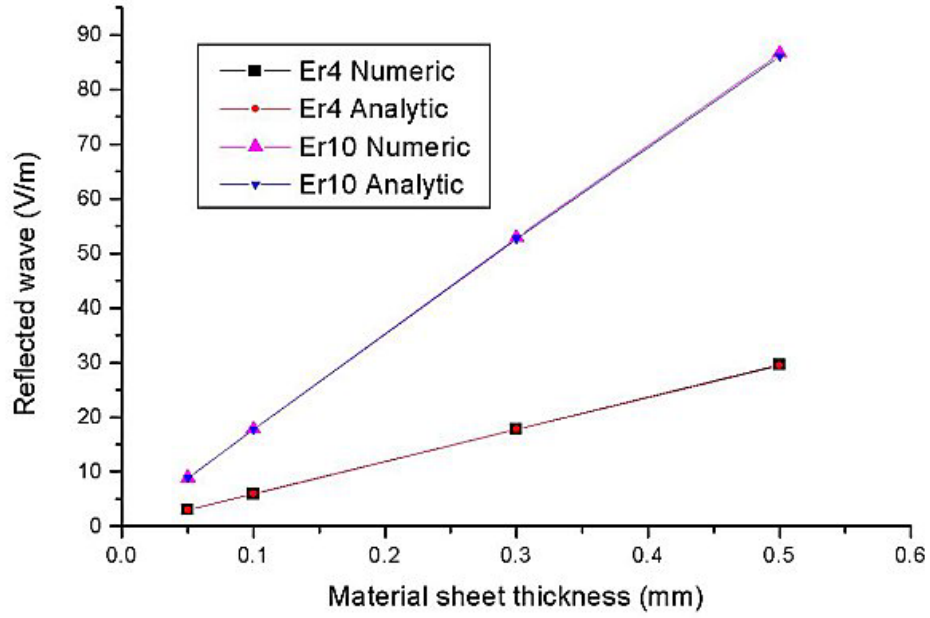
Figure 6.5 Result validation for lossless sheet model

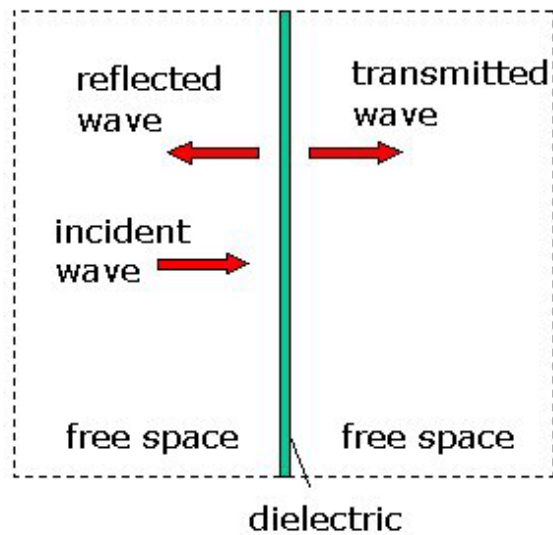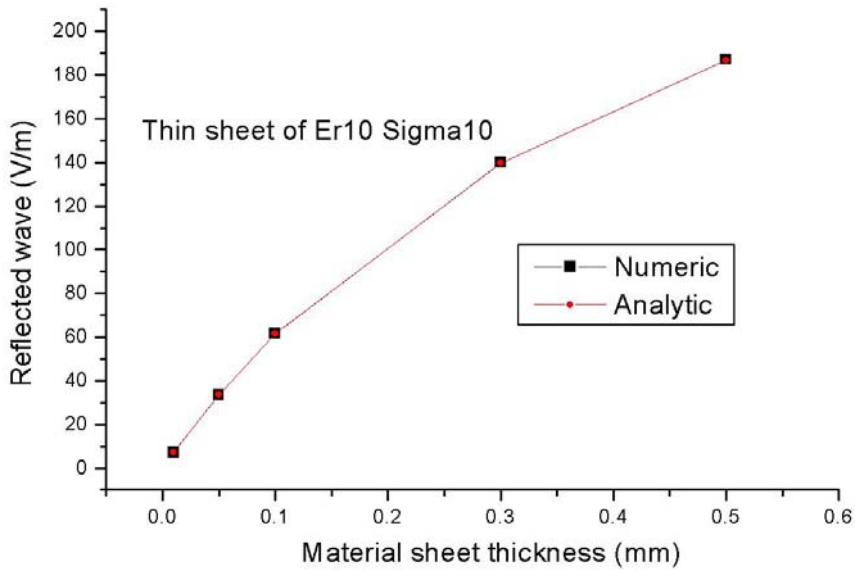

Figure 6.6 Result validation for lossy material model

The above results demonstrate that the code works fine for the model that thin material sheet in free space. However, it should be noted that the incident wave is

normal to the sheet in these models. We need to validate the code to work with oblique incident TE wave. I will measure the reflected wave from a lossy material sheet of ε_r=10, σ=10 $\Omega^{-1}m^{-1}$ where incident wave at 5GHz coming in 45° as in Fig. 6.7. The amplitude of incident wave is the same as the previous models.
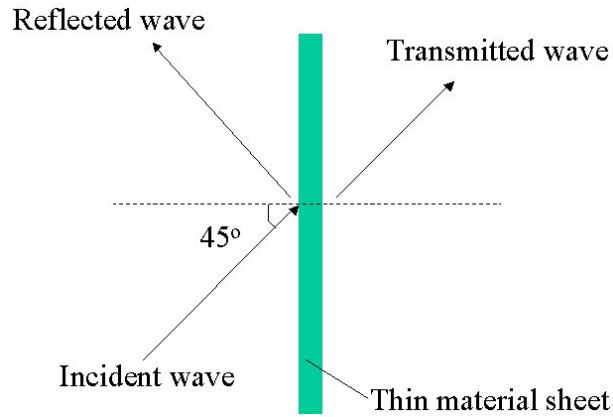
Figure 6.7 Incident wave with 45° angle

The benchmark analytic solution is derived by the boundary condition equations. The numerical result corresponds to the analytic solution very well. This 2D FDTD code works very well to model thin material sheet of any material property and thickness, immersed into free space or other medium.

Figure 6.8 Result validation for oblique incident model

Chapter 7 Conclusions

Numerical and experimental study of resonant cavity and aperture is implemented. The numerical method is developed to calculate S-parameters based on Finite Difference Time Domain simulation. By selectively placing the absorbing material inside of an enclosure, the resonance characteristics of the enclosure are changed.
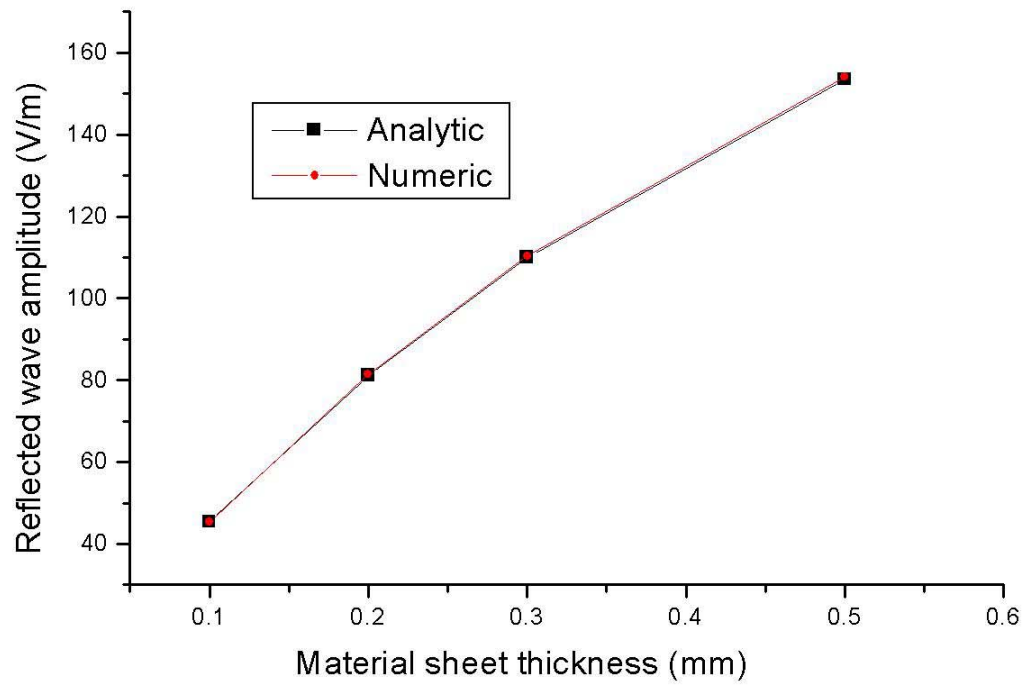
The aperture's radiation is the dominant path for the electromagnetic energy inside of an enclosure to be transmitted to the outside. The model of a 2mm by 20mm aperture on an infinitely large 2mm thick perfectly conducting plane is build by Finite Difference Time Domain tool. I developed the novel technique of applying the absorbing material to the aperture to mitigate electric field penetration. Different size, shape, and configurations of absorbing material are simulated to get the optimal choice. The effect of material width, permittivity and conductivity is numerically solved based on the best configuration chosen at the previous step.

To demonstrate the effectiveness of this technology, a stainless steel rectangular enclosure is built with one aperture 4mm by 40mm large. Two varieties of commercially available material, one dielectric and one magnetic, are applied to the aperture following the best configuration from numerical result. The near field in front of the aperture is evaluated by induced voltage from a receiving monopole antenna. The antenna factor is calculated using equation assuming ideal quarter-wavelength monopole. S-parameters measured using vector network analyzer and the monopole is demonstrated to be an efficient alternative of field strength measurement.

All of the absorbing materials loading reduce the radiation as much as 10 dB. The susceptibility tests for the materials are also implemented. The material loadings reduce of the voltage coupled into the enclosure as much as 10 dB.

Reference

[1]   Christiaan Huygens and Traité de la Luminère (Leyden, 1690), In Scientific Memoirs, pp. 3-41.

[2]   Henry Crew, Scientific Memoirs: The Wave Theory of Light, American Book Corp., Chicago, 1900.

[3]   H. A. Bethe, "Theory of diffraction by small holes," Phys. Rev., vol. 66, pp. 163-182, 1944.

[4]   D.A. Hill, M.T. Ma, A. R. Ondrejka, B.F. Riddle, and M. L. Crawford, "Aperture excitation of electrically large, lossy cavities," IEEE Trans. Electromagnetic Compatibility, vol. 36, no.3, pp. 169-178, Aug. 1994.

[5]   Henry W. Ott, Noise Reduction Techniques in Electronic Systems, 2nd ed. New York: Wiley, 1998.

[6]   R. F. Harrington and J. R. Mautz, "A generalized network formulation for aperture problems," IEEE Trans. Antennas Propagat., vol. 24, no. 6, pp. 870-873, Nov. 1976.

[7]   C. M. Butler, Y.Rahmat-Samii and R. Mittra, "Electromagnetic penetration through apertures in conducting surface," IEEE Trans. Antennas Propagat., vol. 26, no. 1, pp 82-93, Jan. 1978.

[8]   C. L. Gardner and G. I. Costache, "The penetration of EM waves through loaded apertures," IEEE Trans. Electromagnetic Compatibility, vol. 37, no. 3, pp. 358-366, 1995.

[9]   M. P. Robinson, T. M. Benson, C. Christopoulos, J. F. Dawson, M. D. Ganley, A. C. Marvin, S. J. Porter and D. W. P. Thomas, "Analytical formulation for the shielding effectiveness of enclosures with apertures," IEEE Trans. Electromagnetic Compatibility, vol. 40, no.3, pp. 240–248, Aug. 1998.

[10] I. Belokour, J. LoVetri and S. Kashyap, "A higher-order mode transmission line model of the shielding effectiveness of enclosures with apertures," EMC International Symposium on Electromagnetic Compatibility, vol. 2, pp. 702-707, 13-17 Aug. 2001.

[11] G. Cerri, R. De Leo and V. M. Primiani, "Theoretical and experimental evaluation of the electromagnetic radiation from apertures in shielded enclosures," IEEE Trans. Electromagnetic Compatibility, vol. 34, no. 4, pp. 423–432, Nov. 1992.

[12] S.V. Georgakopoulos, C.R. Birtcher and C.A. Balanis, "Coupling modeling and reduction techniques of cavity-backed slot antennas: FDTD versus measurements," IEEE Trans. Electromagnetic Compatibility, vol. 43, no. 3, pp. 261–272, Aug. 2001.

[13] F. Olyslager, E. Laermans, D. De Zutter, S. Criel, R. De Smedt, N. Lietaert and A. De Clercq, "Numerical and experimental study of the shielding effectiveness of a metallic enclosure," IEEE Trans. Electromagnetic Compatibility, vol. 41, no. 3, pp. 202–213, Aug. 1999.

[14] M. Li, J. Nuebel, J. L. Drewniak, R. E. DuBroff, T. H. Hubing and T. P. VanDoren, "EMI from cavity modes of shielding enclosures-FDTD modeling and

measurements," IEEE Trans. Electromagnetic Compatibility, vol. 42, no. 1, pp. 29–38, Feb. 2000.

[15] M. Li, J. Nuebel, J. L. Drewniak, T. H. Hubing, R. E. DrBroff and T. P. Van Doren, "EMI from airflow aperture arrays in shielding enclosures—experiments, FDTD, and MoM modeling," IEEE Trans. Electromagnetic Compatibility, vol. 42, no. 3, pp. 265–275, Aug. 2000.

[16] S. Tanabe, N. Nagano, T. Itoh, Y. Murata and S. Mizukawa, "3D-FEM analysis for shielding effects of a metallic enclosure with apertures," IEEE International Symposium on Electromagnetic Compatibility, pp. 375-380, 19-23 Aug. 1996.

[17] B. Archambeault, Modeling of the Electromagnetic Radiation from Shielded Enclosures with Apertures and Attached Wires in a Real-World Environment, Ph.D. Dissertation, University of New Hampshire, 1997.

[18] M. Li, J. Nuebel, J. L. Drewniak, R. E. DuBroff, T. H. Hubing, and T. P. VanDoren, "EMI from cavity modes of shielding enclosures-FDTD modeling and measurements," IEEE Trans. Electromagnetic Compatibility, vol.42, pp. 29–38, Feb. 2000.

[19] M. Li, J. L. Drewniak, T. H. Hubing, and T. P. VanDoren, "Slot and aperture coupling for airflow aperture arrays in shielding enclosure designs," in Proc. IEEE Electromagnetic Compatibility Symposium, Seattle, WA, 1999, pp. 35–39.

[20] U.S. Department of Defense Multi-University Research Initiative Program on Effects of Radio Frequency Pulses on Electronic Circuits and Systems (http://www.ireap.umd.edu/MURI-2001/)

[21] Min Li, Joe Nuebel, James L. Drewniak, Todd H. Hubing, Richard E. DuBroff and T. P. Van Doren, "EMI reduction from airflow aperture arrays using dual-perforated screens and loss," IEEE Trans. Electromagnetic Compatibility, vol. 42, no. 42, pp. 135-141, May 2000.

[22] P. M. Goggans and T. H. Shumpert, "Backscatter RCS for TE and TM Excitations of Dielectric-Filled Cavity-Backed Apertures in Two –Dimensional Bodies," IEEE Transaction of Antennas and Propagation, Vol. 39, No. 8, August 1991

[23] C. A. Balanis, Advanced Engineering Electromagnetics, John Wiey & Son, 1989.

[24] EZ-FDTDTM, a Three-Dimensional Full-Wave Analysis Tool, EMS-PLUS, LLC.

[25] W. T. Cathey, "Approximate expression for field penetration through circular apertures," IEEE Trans. Electromagnetic Compatibility, Aug. 1983, pp. 339–345.

[26] S. V. Savov, "Mutual coupling between two small circular apertures in a conducting screen," IEEE Trans. Microwave Theory Tech., vol. 41, pp. 143–146, Jan. 1993.

[27] Y. B. Park and H. J. Eom, "Electromagnetic transmission through multiple circular apertures in a thick conducting plane," IEEE Transactions on Antennas and Propagation, Vol. 52 , No.4 , April 2004, pp.1049-1055.

[28] T. T. Wu and R. W. P. King, "The cylindrical antenna with nonreflecting resistive loading," IEEE Trans. Antennas Propagat., vol. 13, no. 1, Jan. 1965

[29] H. Moheb, L. Shafai, and J. Shaker, "Numerical solution of radiation from single and multiple arbitrary apertures backed by a cavity", Antennas and Propagation Society International Symposium, 1992 Digest, vol. 1, pp. 61-64, 1992.

[30] S. Daijavad and B.J. Rubin, Modeling common-mode radiation of 3D structures, IEEE Transactions on Electromagnetic Compatibility, Vol. 34, pp. 57-61, Feb. 1992.

[31] S. Hashemi-Yeganeh and C. Birtcher, "Theoretical and Experimental Studies of Cavity-Backed Slot Antenna Excited by a Narrow Strip," IEEE Transaction on Antennas and Propagation, Vol. 41, No. 2, Feburary 1993.

[32] B. Audone and M. Balma, "Shielding Effectiveness of Apertures in Rectangular Cavities," IEEE Transaction on Electromagnetic Compatibility, Vol 31, No. 1, February 1989.

[33] M. Li, K. Ma, D. M. Hockanson, J. L. Drewniak, T. Hubing, and T. P. Van Doren, "Numerical and Experimental Corroboration of an FDTD Thin-Slot Model for Slots Near Corners of Shielding Enclosures," IEEE Transaction on Electromagnetic Compatibility, Vol 39, No. 3, August 1997.

[34] P. Sewell, J. D. Turner, M. P. Robinson, T. M. Benson, C. Christopoulos, J. F. Dawson, M. D. Ganley, A. C. Marvin, and S. J. Porter, "Comparison of Analytic, Numerical and Approximate Models fro Shielding Effectiveness with Measurement," IEE Proceedings Science, Measurement & Technology, Vol. 145, No. 2, March 1998.

[35] A. C. Polycaropu, C. A. Balanis, J. T. Aberle, and C. Birtcher, "Radiation and Scattering from Ferrite-Tuned Cavity-Backed Slot Antennas: Theory and Experiment," IEEE Transaction on Antennas and Propagation, Vol. 46, No. 9, September 1998.

[36] K. Chamberlin and L. Gordon, "Modeling good conductors using the finite-difference, time-domain technique," IEEE Transactions on Electromagnetic Compatibility, Volume 37, Issue 2, May 1995.

[37] J. G. Maloney and G. S. Smith, "The use of surface impedance concepts in the finite-difference time-domain method," IEEE Transactions on Antennas and Propagation, Volume40, No.1, January 1992.

[38] S. V. den Berghe, F. Olyslager, and D. Zutter, "Accurate modeling of thin conducting layers in FDTD," IEEE Microwave and Guided Wave Letters, Vol. 8, No. 2, February 1998.

[39] R. J. Luebbers and K. Kunz, "FDTD modeling of thin impedance sheets," IEEE Transactions on Antennas and Propagation, Volume 40 Issue 3, March 1992.

[40] J. G. Maloney and G.S. Smith, "The efficient modeling of thin material sheets in the finite-difference time-domain (FDTD) method," IEEE Transactions on Antennas and Propagation, Volume 40 Issue 3, March 1992.